Imaging Skins and Threads: An Exploration of Far-field Optical Imaging Systems Confined to a Two-dimensional or One-dimensional Form-factor

A DISSERTATION

SUBMITTED TO THE FACULTY OF THE GRADUATE SCHOOL

OF THE UNIVERSITY OF MINNESOTA

BY

Jordan Benjamin Burch

IN PARTIAL FULFILLMENT OF THE REQUIREMENTS

FOR THE DEGREE OF

Doctor of Philosophy

James R. Leger

August, 2016

Acknowledgements

The surface relief gratings were fabricated in collaboration with Ying Wan.

The prism coupler imaging experiment was performed in collaboration with Molly Krogstad.

Special thanks to Junying Zhang and Terry Smith for producing planar waveguide material and Jacques Albert for fabricating the tilted fiber Bragg gratings.

Thank you to all the my fellow graduate students who provided proof-reading, countless conversations, and boundless encouragement without which this work would not have been possible: Brad Tiffany, Mint Kunkel, Merlin Mah, Andrew Brown, and Lucas Taylor.

Dedication

To all the teachers who believed in me, even when I didn't believe in myself.

Abstract

The resolution diffraction limit of an imaging system is inversely proportional to the width of its aperture. The depth of these systems, however, is determined by the choice of architecture. To show that an imaging system can be confined to a plane or a line, while maintaining high far-field resolution, two new architectures are presented. The planar device, referred to as an imaging skin, uses a grating coupler to map points in the far-field to guided modes in a slab waveguide. Similarly, an imaging thread is a nearly one-dimensional device which uses a tilted fiber Bragg grating to couple points into a guided mode of an optical fiber. The diffraction gratings introduce a high degree of chromatic aberration. To maintain their resolution, imaging skins and threads must use a narrow spectral filter. When these devices are used at finite conjugates, only sources very near the object plane have high coupling efficiency. Both systems, despite their extreme form factors, are shown to have far-field resolution near the diffraction limit of a lens with a similar diameter.

Contents

List of Tables

List of Figures

Chapter 1

Introduction

Size and weight constraints are often limiting factors for imaging systems. For example, the added weight of a camera on a drone can significantly decrease the useful range and agility. In medicine, an ingestible camera must be small enough to not become lodged in the digestive track. In the surveillance applications, the goal is often to be as inconspicuous as possible. Thin and light cameras could potentially be adhered to surfaces making them very difficult to spot. The preference for smaller form factors is also evident in the consumer market. Cell phone cameras, despite their lower resolution and restriction to wide angle lenses, have largely replaced mid-range digital cameras. Reduction in the size and weight of imaging systems could enable countless new applications.

The history of optical imaging has had many paradigm shifts which have allowed for ever smaller systems. During this development, fundamental limits on aperture length and width have been described. The depth of the these systems depended on the particular modality and a fundamental minimum has yet to be determined. Different imaging architectures, with the accompanying size constraints, are reviewed.

1.1 Pinhole Camera

One of the earliest, man-made imaging systems was the camera obscura. In these devices, a narrow cone of light enters through a small pinhole, in an otherwise dark enclosure, and projects an image on the wall. In practice, the depth of these systems is determined by the required magnification given by

$$m = -\frac{d_i}{d_o}, \tag{1.1}$$

where d_i and d_o are the image and object distance respectively. If the film grain or pixel pitch could be made arbitrarily small, the magnification becomes far less important. It has been known since the 1890s [1] that to maximize resolution, the distance from the hole to the wall, d_i is

$$d_i = 2r^2/\lambda \tag{1.2}$$

where r is the radius of the hole and λ is the wavelength of light. Decreasing the radius of the pinhole will reduce required image distance, however the optical throughput is proportional to the radius squared. The minimum received power, therefore, sets the fundamental minimum on the system depth for pinhole cameras.

1.2 Refractive Lenses and Mirrors

Compared to a pinhole camera, lens and mirror systems have vastly improved optical throughput for a given resolution. This comes from the ability of refractive elements to focus all rays which cross their aperture into a sharp focus. Under the Rayleigh criterion, the minimum distance between two resolvable spots is

$$r = \alpha\frac{\lambda}{2NA}, \tag{1.3}$$

where α is a constant based on the pupil geometry. Specifically, α is 1 and 1.22 for a square and circular aperture respectively. The numerical aperture for a lens is

$$NA = n\frac{D}{\sqrt{D^2 + 4d_0^2}}, \tag{1.4}$$

where D is the lens diameter. Based on Eqs. 1.3 and 1.4, relatively high spatial resolution can be achieved with modest lens diameters by moving the object close to the lens. For example, a typical microscope objective with a $NA = 0.4$ might have a $1\,mm$ diameter, but requires the object distance to be $1.2\,mm$. For imaging at a significant distance, there is no substitute for aperture size. Angular resolution of any imaging system, so long as that system relys only on propagating waves, has a diffraction limit proportional to the lateral extent of the pupil [2].

The diffraction limit sets the minimum length and width of the pupil, but not the depth of the total system. The thickness of an imaging system includes both the image distance and the thickness of the lens material. These two lengths are not independent and, therefore, cannot simultaneously be made arbitrarily small. For a refractive lens, the minimum total system thickness is proportional to the lens diameter as shown in appendix A. In that analysis, the system is an infinite-conjugate imaging system using a single plano-convex lens. Finite conjugate systems or systems with a biconvex lens would have slightly different scale factors, but the same linear dependence. The minimum thickness, normalized by the lens diameter, for different indices is shown in Fig. 1.1. Increasing the refractive index can reduce the system thickness, but the range of refractive indices for lens material is quite limited. According to the Kramer-Kronig relations, materials with high index also tend to be high loss. For most glasses, with the index around 1.5, the minimum image distance is approximately equal to the lens diameter.

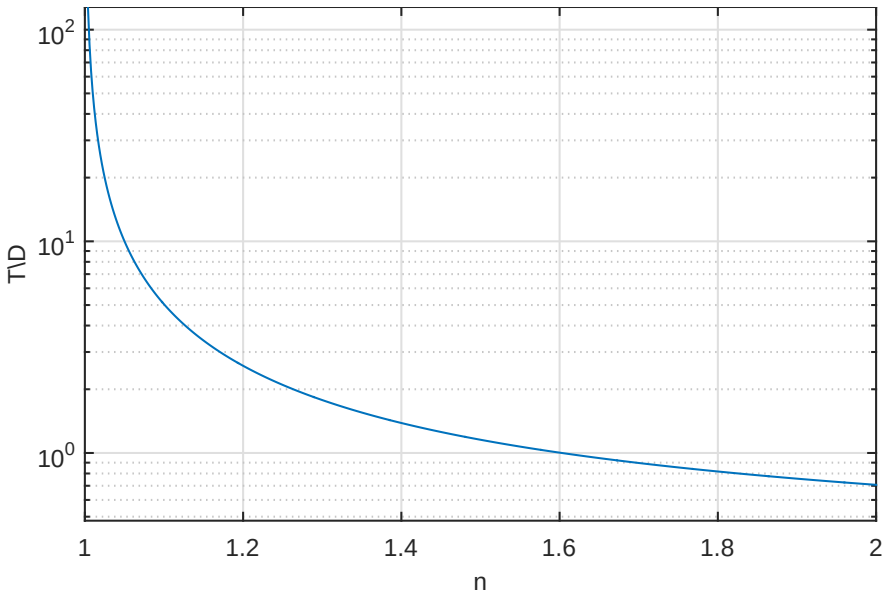

Figure 1.1: Minimum thickness (T), normalized by lens diameter (D), for an infinite-conjugate imaging system with a single plano-convex lens of refractive index n

1.3 Aberrations

In addition to the fundamental minimum system thickness, the allowable degree of aberration may set a practical limit. As the image distance decreases, aberrations tend to increase. Specifically, spherical aberration, the dominant on-axis aberration for a spherical lens, increases as $\frac{D^3}{f^2}$, where f is the focal length and D aperture diameter. To prevent large spherical aberrations, the image distance should be greater than $D^{3/2}$. An asphere can be designed to have no spherical aberration, but doing so invariably increases off-axis aberrations. To minimize all aberrations simultaneously, a lens designer typically uses a stack of lens elements. The number of optical surfaces can range from a few in a commercial camera to many hundreds in an optical lithography system. Multi-lens systems yield well-focused spots over a wide field of view, but tend to be long, heavy, and expensive.

1.4 Folded Optics

There exists a class of imaging systems which use multiple mirrors to reduce sytem thickness. The Cassegrain telescope is a classic example of these folded-optic systems. Whereas a Newtonian telescope uses a flat mirror to couple light out the side of the tube, a Cassegrain has a small convex secondary mirror which reflects the light through a small hole in the primary [3]. As a result, a Cassegrain can have half the tube length for the same effective focal length. Enabled by the development of high resolution diamond turning, this technique was expanded by Ford to an 8 fold system [4]. In that implementation, light enters through an annular aperture on the periphery and, through successive reflections, propagates to a CCD in the center. The total thickness of a folded system is inversely proportional to the number of reflections.

Though effective for moderate numbers of reflections, the thickness of a folded-optic system can not scale indefinitely. In both the Cassegrain and Ford architectures, a portion of the entrance pupil is occluded by the later reflecting optics. The portion of the aperture that is obscured is linearly proportional to the number of folds. Therefore, as the device becomes thinner, the less contrast is available in the mid frequencies. The optical throughput also decreases as the device becomes thinner. Assuming each of the N surfaces has a reflectance R, the power efficiency is

$$\eta = R^N. \tag{1.5}$$

The efficiency vs normalized thickness is shown in Fig. 1.2. Consider a folded system which uses silvered mirrors with reflectance of 97.5%. A $100x$ reduction in depth results in 90% power loss. To get down to 1/1000 the image distance, the power is decreased by 120 dB. Even with very high reflectance, the power efficiency drops quickly as the depth approaches zero.

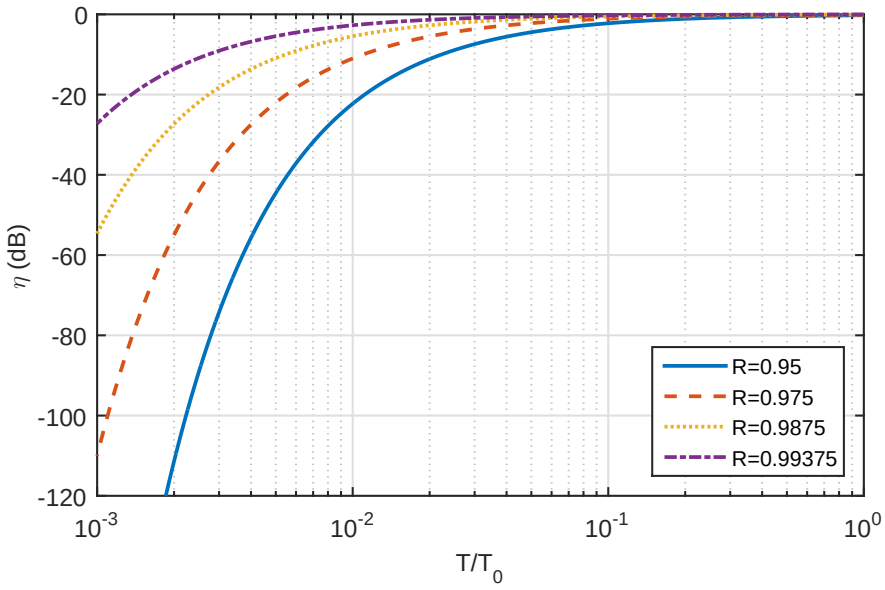

Figure 1.2: Efficiency vs thickness for folded optic system

1.5 Diffractive Optics

Though folded systems are effective at reducing the effective image distance, the added mirror surfaces tends to increase the system weight. Diffractive optics, in some sense, are their opposite. Diffractive lenses are thin and light, but provide no reduction in image distance. Within the framework of Fourier optics, an object which has the 2π modulus of the phase behaves equivalently to an object with phase unwrapped. Therefore, for a single spectral frequency, any phase function can be encoded in a piece of dielectric which is one wavelength thick.

Harmonic lenses, like the one shown in Fig. 1.3, are far thicker than a wavelength. By using the modulus of $M2\pi$, where M is a positive integer, the zone areas become larger significantly decreasing fabrication complexity. Harmonic lenses also have lower chromatic dispersion compared to a first order lens [5]. Diffractive lenses allow a designer to trade-off chromatic dispersion and fabrication ease for a for lens thickness and weight.

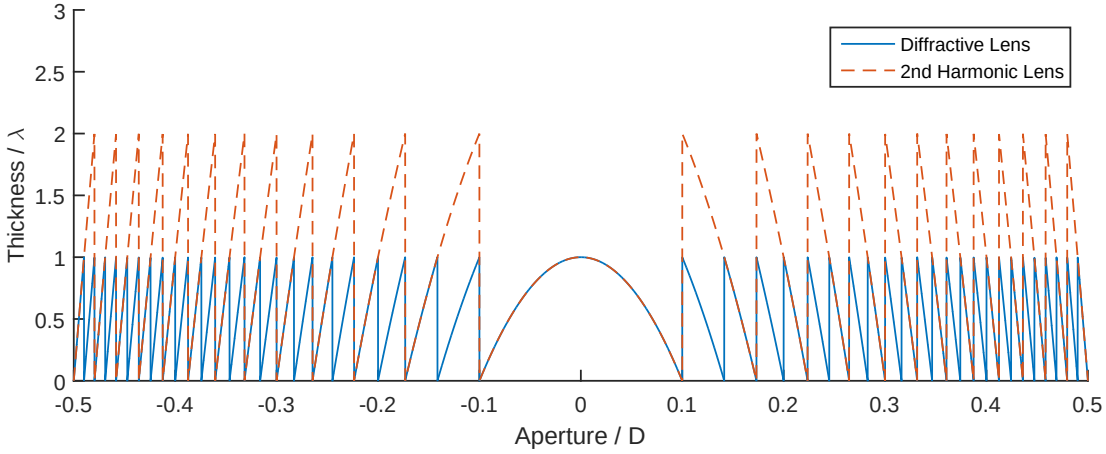

Figure 1.3: Diffractive and harmonic lens

1.6 Confocal Imaging

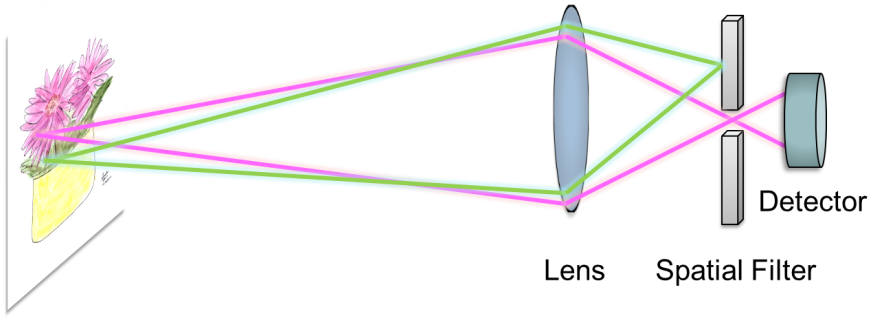

Figure 1.4: Confocal imaging system

A confocal system does not have a particularly small form-factor, but this imaging architecture is reviewed because it is useful in describing the proposed imaging threads and skins. In confocal imaging, shown in Fig. 1.4, the detector is moved away from the lens and a spatial filter is placed in the image plane. Source points not on the object

plane are out of focus at the pinhole so only a small portion of their power reaches the detector. By translating the object along the imaging axis, a confocal systems can measure the objects surface topography. Although three-dimensional imaging is the most common application for confocal imaging, it is also worth noting that the spatial filter decouples the lateral resolution of the system from the area of the detector. Whereas all image points are recorded simultaneously in a standard camera, only a single object point passes through the aperture at a time in a confocal system. A single bulk detector can then be used, but the system must then be scanned to image an entire object.

1.7 Angle Filter Based Imaging

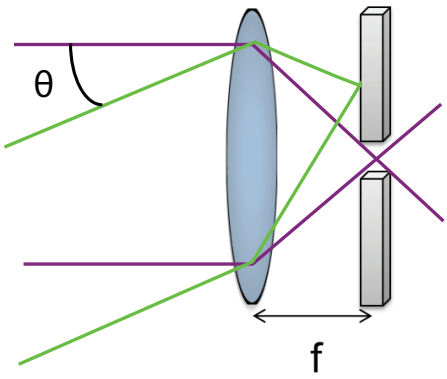

Figure 1.5: Confocal system configured as an angle filter

When the pinhole in a confocal system is moved to the back focal plane of the lens, as shown in Fig. 1.5, the object plane moves to infinity. Equivalently, only light in a very narrow cone of angles is detected. Other examples of optical devices which filter by angle include volume holograms [6], Fabry-Perot etalons [7], and birefringent crystals with a linear polarizer. Any of these devices could be considered an infinite conjugate imaging

system, but the angle resolution of these other filters depends on their thickness. As will be demonstrated, grating couplers on a single mode waveguide can have high far-field resolution with a system thickness on the order of a few wavelengths. Most importantly, it will be shown that the angle resolution is independent of system thickness.

This work is an exploration of the limits on the form-factor of an optical imaging system given a resolution requirement. According to Fourier optics, the far-field resolution of any imaging system, at least any which relies on only propagating waves, has a diffraction limit proportional to the lateral extent of the pupil [2]. Therefore, reducing any spatial-dimensions on which the required resolution does not depend can decrease the weight and cost of the system. Throughout the history of the field, new architectures and technologies in optical imaging have allowed designers to reduce system depth and weight, but always at the expense of some other performance metric. In the same spirit, a new architecture based on waveguide grating-couplers is presented. In addition to the first demonstrated images, the design considerations and fundamental limits of the technique are presented.

Chapter 2

Imaging Skins

Imaging skins are here defined as the class of high resolution imaging systems which are restricted to a plane. It is likely that this class has many members, but this work will focus on a single architecture which uses a grating coupler on a planar waveguide. A grating coupler is any periodic variation in waveguide refractive index which couples energy from a guided to a radiation mode, or vise-versa [8]. Though they are common in the field of integrated optics, grating couplers have not previously been used as an imaging device. A first step is to describe the system in the imaging system framework. Specifically, the point spread function of a grating coupler is calculated and experimentally verified. Whereas most grating couplers are relatively short to ease alignment tolerances, the grating length in the imaging skin is proportional to the desired resolution. Design considerations unique to long gratings are presented. Finally, an image of a pseudo-random barcode will be used as a proof of the concept.

An illustration of the proposed system is shown in Fig. 2.1. Consider a guided mode propagating in the planar waveguide. When the light reaches the grating, the guided mode couples into a radiating wave within a narrow angle cone. Reversing the direction of propagation, light entering at the same angle will couple into the guided

mode and propagate to a detector. If the input angle is mismatch, a leaky mode is excited. Therefore, only angles within a narrow cone are detected. An image can then be formed by scanning over the object.

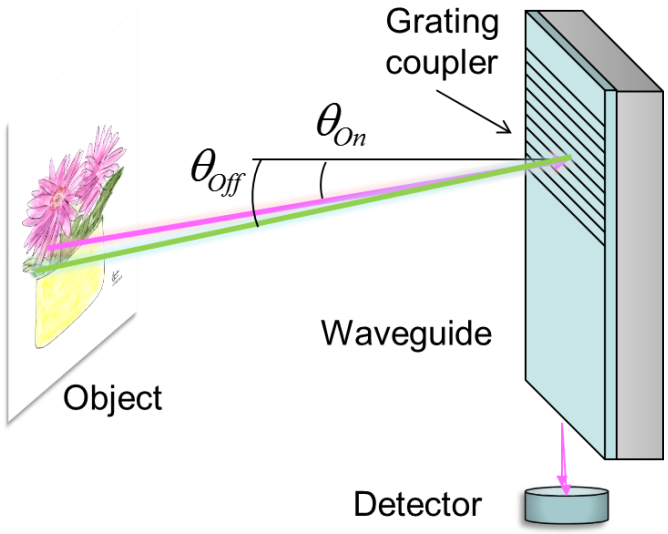

Figure 2.1: Illustration of imaging with grating coupler

The waveguide-grating structure is quite analogous to a confocal system. Similar to the lens mapping position in the far-field to points in the image plane, the grating maps angles in free space to "points" in the waveguide mode domain. Akin to the pinhole filtering in the image plane, the mode structure of the guide filters in mode space. Whereas the spatial filter may be enlarged to trade-off resolution for optical throughput, the waveguide modes are essentially delta functions. For a single mode guide, like a single aperture confocal system, a single detector can be used. Both systems must be scanned to build an image. As describe previously, the conjugate ratio of a confocal system can be changed by translating the pinhole with respect to the lens. One can move from infinite to finite conjugates by adding a chirp to the grating period as described in chapter 6. For now, the system is assumed to be infinite conjugate with

uniform period gratings.

Several varieties of grating couplers have been developed. Types of gratings include thin [9] and volume [10] holographic in photo-polymer, and surface relief. Unless otherwise specified, a binary surface relief grating will be assumed. Since we are concerned with making the system as light as possible, air will be chosen as the superstrate. The waveguide-grating structure, with these assumptions, is illustrated in Fig. 2.2.

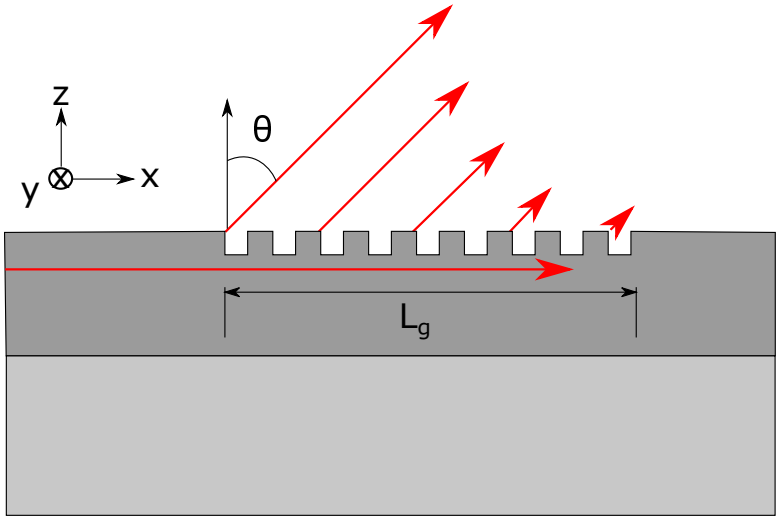

Figure 2.2: Mode out-coupling from grating

2.1 Angular Resolution

The angle spread function (ASF), the infinite conjugate analog to the point spread function, completely describes an imaging system within the framework of Fourier optics. Specifically, the image is given by the convolution of the ASF with the angular plane wave spectrum of the object. The width of the ASF determines system resolution and will be determined analytically and confirmed experimentally.

According to reciprocity, the input angle acceptance of any optical system is equal to the angle spread of the output. To determine the ASF of the imaging skin, the

radiating field from a mode out-coupling through the grating is calculated. For now, the mode will be assumed to be uniform in the y-direction and propagating only in the x and z-directions as shown in Fig. 2.3. In this case, the ASF is variable separable and can be written as

$$\mathcal{A}(\theta_x, \theta_y) = \mathcal{A}_x(\theta_x) \times \mathcal{A}_y(\theta_y), \tag{2.1}$$

where the x and y-directions can be calculated independently.

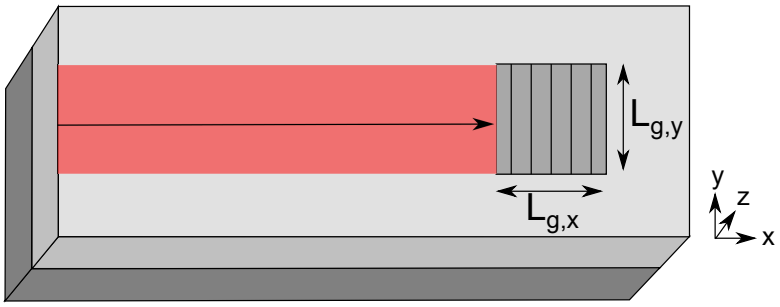

Figure 2.3: Mode uniform in y-direction

The out-coupling of power is proportional to the mode's power at each location within the grating region [11]. Beyond the grating, $|y| > L_{g,y}/2$, no additional light is coupled and the field is zero. The y-direction term of the field just outside grating is

$$A_y(y) = A_{0,y}\text{rect}\left[\frac{y}{L_{g,y}}\right], \tag{2.2}$$

where $A_{0,y}$ is a scalar constant. The corresponding ASF term is found by taking a Fourier transform. After substituting the Fourier conjugate variable with θ_y/λ, the y-direction term of the ASF is

$$\mathcal{A}_y(\theta_y) = A_{0,y}L_{g,y}\text{sinc}\left[\frac{L_{g,y}}{\lambda}\theta_y\right]. \tag{2.3}$$

In the y-direction, the angle spread function is the same as a diffraction limited lens with diameter $L_{g,y}$.

If the grating is uniform (same period and depth) across its entire length $L_{g,x}$, the change in mode power in the x-direction is a first order differential equation with constant coefficients. Light, after being coupled to a radiating mode, cannot rejoin the guided mode. The general solution of this ODE which monotonically decreases is the decaying exponential. The exponential decay length of the mode amplitude is defined to be L_c, so the mode power decreases to $1/e^2$ when $x = L_c$. The complex amplitude of the radiating field in the x-direction just outside the grating is

$$A_x(x) = A_{0,x} \exp\left[-\frac{x + (L_g \cos\theta_0)/2}{L_c \cos\theta_0}\right] \times \text{rect}\left[\frac{x}{L_g \cos\theta_0}\right], \tag{2.4}$$

where $A_{0,x}$ is magnitude of the amplitude at $x = -L_{g,x}/2$. The $\cos\theta_0$ term has been added to account for the projected lengths resulting from the radiating mode out-coupling at the angle θ_0 with respect to the waveguide surface normal. An example normalized profile is shown in figure 2.4. The x-component angle spread function is calculated by performing a Fourier transform on Eq. 2.4. After substituting the Fourier conjugate variable with θ_x/λ the ASF is

$$\mathcal{A}_x(\theta_x) = A_{0,x} \frac{2\exp\left(\frac{-L_g}{2L_c}\right)\sinh\left(\frac{-L_g}{2L_c} + \frac{\imath\pi L_g \cos\theta_0}{\lambda}\theta_x\right)}{\frac{1}{L_c\cos\theta_0} + \frac{\imath 2\pi}{\lambda}\theta_x}. \tag{2.5}$$

A similar analysis calculates the acceptance angle when a known Guassian beam is coupled into a planar waveguide by a grating coupler [12]. The results of that analysis, however, are only given in the extreme cases where either L_g, L_c, or the incident beam width are significantly smaller than the other two lengths. If the coupling length is much larger than the grating length, Eq. 2.5 approaches the diffraction pattern from a rectangular aperture,

$$\lim_{L_c\to\infty} \mathcal{A}_x(\theta_x) = A_{x,0} \frac{\lambda \sin\left(\pi \frac{L_{g,x}}{\lambda}\theta_x\right)}{\pi\theta_x}. \tag{2.6}$$

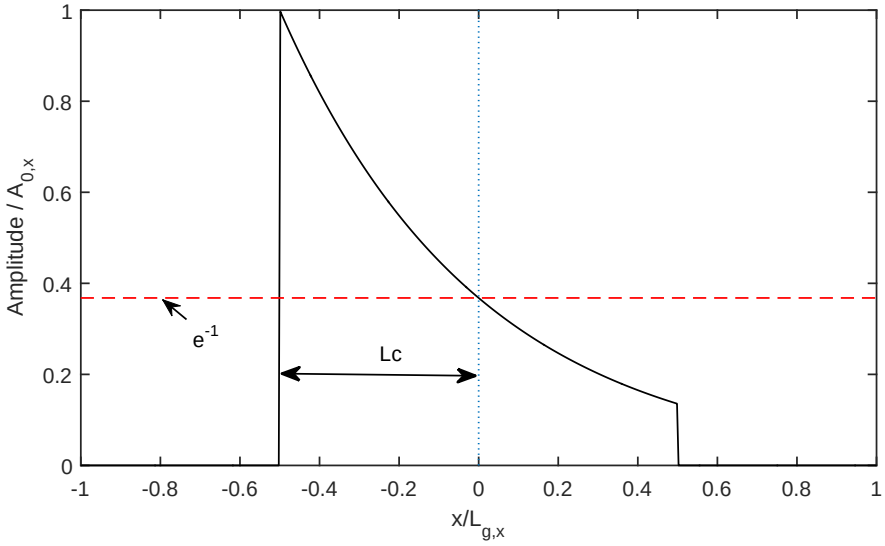

Figure 2.4: Example normalized complex amplitude just outside of the grating

In the opposite case, $L_c << L_g$, the ASF becomes more like a Lorentzian. These extreme cases match the results given in [12]. It is shown in section 2.2 that the coupling and grating lengths must be approximately equal to maximize coupling efficiency. Fig. 2.5 plots Eq. 2.5 where $L_g = L_c$. The sinc-squared function, corresponding to the same grating length, but $L_c = \infty$, is also plotted for comparison. Though the shape of the curves are different, the width of the central peaks are essentially the same. In all cases, the width of the ASF is inversely proportional to the smaller of the coupling or grating lengths.

2.2 Coupling Efficiency

In integrated optics, a grating is used to efficiently couple optical power into a waveguide. The coupling efficiency is calculated using mode overlap equation [13],

$$\eta = \frac{\left|\int A^*(x,y)B(x,y)dS\right|^2}{\int |A(x,y)|^2\, dS \cdot \int |B(x,y)|^2\, dS}, \tag{2.7}$$

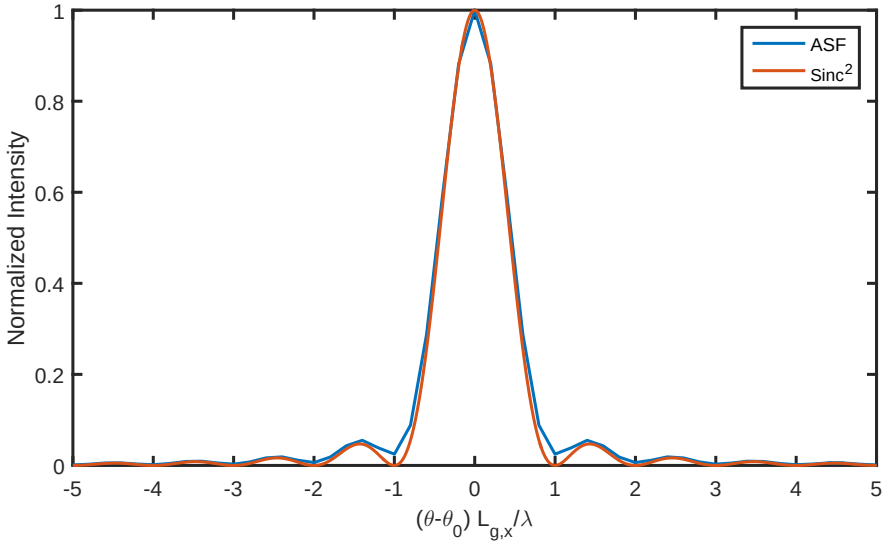

Figure 2.5: Normalized ASF with Sinc function

where $*$ indicates the complex conjugate, dS is the infinitesimal area element, A is the complex amplitude of the ideal out-coupling field, and B is the field from the object in the grating plane. Any unitary operator, including the Fourier transform, preserves the inner product of any two vectors in a Hilbert space. Therefore, the overlap integral can equivalently be performed in the angle domain. To use the grating as an imaging device, the object plane must be scanned and the integral in the numerator of Eq. 2.7 becomes a convolution. To calculate the power at each scan location, the efficiency is multiplied by the total object power. With these two modifications, convolution with a point spread function and the overlap integral are different expressions of the same theory. Whereas the linear system theory is useful for describing its imaging performance, the coupled-mode theory will give insight into the design of a grating-coupler based imaging system.

For an infinite conjugate imaging skin, the coupling efficiency is to be maximized for a single plane wave. As shown in section 2.1, the ASF becomes more narrow as the coupling and grating length increase, but never converge to a delta function for a finite

grating. The overlap integral 2.7 is useful for determining the coupling and grating lengths which maximize coupling efficiency.

A true plane wave has finite energy density but is infinite in extent and total power, so the total efficiency for a finite grating is zero. Instead, the efficiency will be calculated as a fraction of the power which falls within the grating region which enters the waveguide. The object is then assumed to be a truncated plane wave traveling anti-parallel to the out-coupling angle. In this special case, both A and B are variable separable. As a result, the two dimensional integrals in Eq. 2.7 can be written as the product of two one-dimensional integrals. The y-terms are constants which appear in both the numerator and denominator and will be ignored. The efficiency is then

$$\eta = \frac{\left| \int_0^{L_g} B_0 A_0 \exp(-x/L_c) dx \right|^2}{\int_0^{L_g} \left| A_0 \exp(-x/L_c) \right|^2 dx \cdot \int_0^{L_g} \left| B_0 \right|^2 dx}, \tag{2.8}$$

where all variables are the same as defined in section 2.1 but the x-subscript has been dropped. After evaluating the integrals and some simplification, the efficiency is

$$\eta = 2\frac{L_c}{L_g}\left[1 - \exp\left(\frac{-L_g}{L_c}\right)\right]^2. \tag{2.9}$$

The efficiency, as shown in Fig. 2.6, depends on the ratio of coupling length to grating length, but not the individual values. Recall that this is the efficiency of the power within the grating aperture. Assuming the illumination is an unbound plane wave, the total power outside the guide is linearly dependent on the grating length. However, increasing the grating length without a commensurate increase in the coupling length would result in a sub-linear increase in the coupled power.

The imaging skin would ideally have as large an efficiency as possible, so long as increasing the optical throughput does not compromise resolution. Because the efficiency only depends on the ratio of grating to coupling length, it is useful to define a new variable α as

$$\alpha = \frac{L_g}{L_c} \tag{2.10}$$

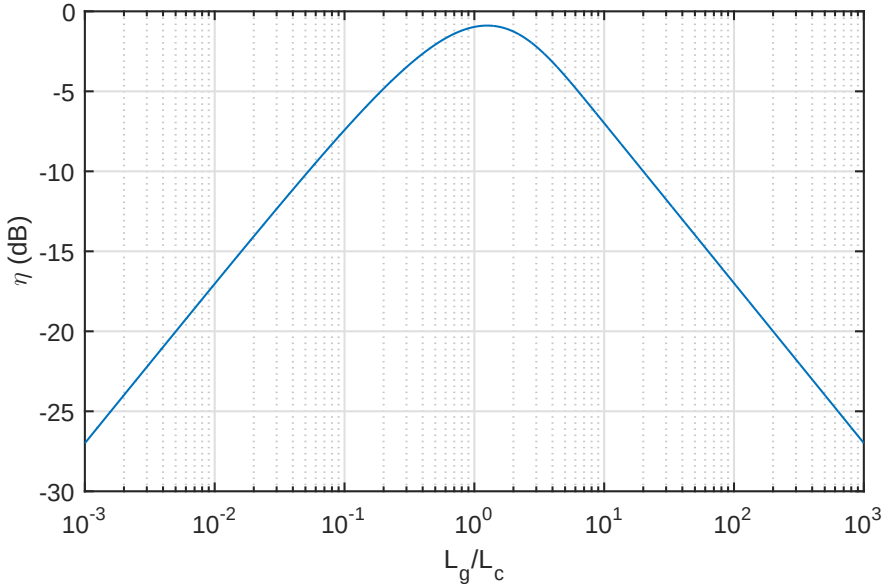

Figure 2.6: Coupling efficiency for a plane wave vs $\frac{L_g}{L_c}$

Setting the derivative of Eq. 2.9 with respect to α to zero yields the transcendental equation

$$\exp \alpha = 1 + 2\alpha, \tag{2.11}$$

the solution to which is $\alpha = 1.25643$. By evaluating Eq. 2.9 at this ratio, the maximum efficiency for a plane wave coupling into a grating coupler is 81.4529% The same numerical results are given in [14]. The efficiency falls to half the maximum, a reasonable design constraint, when $\alpha = 0.2643$ and 4.8205.

According to Fourier optics, a point source at infinity has the same phase as a plane wave at the grating surface. It is interesting to ask how the efficiency of the grating changes as the object point is translated along the optical axis. The overlap integral is evaluated for a point at different object distances. For this analysis, it will be assumed that $\theta_0 = 0$ and z_0 is the distance between the point and the grating surface. The object field at the grating surface has the form of a diverging spherical wave. The efficiency is

given by the overlap integral

$$\eta(z_0) = \frac{\left| \int_{-L_{g,y}/2}^{L_y/2} \int_{-L_{g,x}/2}^{L_{g,x}/2} \exp\left[ik\sqrt{x^2+y^2+z_0^2}\right] \exp\left[-\frac{x+L_{g,x}/2}{L_c}\right] dxdy \right|^2}{\int_{-L_{g,y}/2}^{L_{g,y}/2} \int_{-L_{g,x}/2}^{\infty} \left|\exp[-\frac{x+L_{g,x}/2}{L_c}]\right|^2 dxdy \cdot \int_{-L_{g,y}/2}^{L_{g,y}/2} \int_{-L_{g,x}/2}^{L_{g,x}/2} \left|\exp\left[ik\sqrt{x^2+y^2+z_0^2}\right]\right|^2 dxdy}. \tag{2.12}$$

Because the object distance is much greater than the extent of the grating, one may be tempted to replace the spherical wave with its paraxial approximation. Even the approximate expression does not have an analytic solution, therefore Eq. 2.12 must be calculated numerically for specific values. Setting $L_{g,x} = L_{g,y} = 1\,cm$, $L_c = L_{g,x}/1.25643$, and $\lambda = 632.8\,nm$, the efficiency is calculated for different distances shown in Fig. 2.7. The efficiency is essentially zero when the point is close to the grating because of the large phase mismatch. As z_0 approaches ∞ the field approaches a plane wave and the efficiency approaches the maximum efficiency. The transition occurs when z_0 is close to Rayleigh range,

$$z_R = \frac{\pi L_g^2}{4\lambda}, \tag{2.13}$$

which in this example is $124\,m$.

The efficiency given in Eq. 2.12 is with respect to the total optical power which intersects the grating aperture. The total percentage of power from the point which couples into the guided mode is also an interesting parameter. The intensity of light from a point source decays as the square of the distance. Because the length and width of the grating are small compared to z_0, all points on the grating are assumed to be the same distance from the point. The total power coupled into the mode is

$$P = P_0 \eta(z_0) \frac{L_{g,x} L_{g,y}}{4\pi z_0^2}, \tag{2.14}$$

where P_0 is the total power of the point. This total efficiency is plotted in Fig. 2.8. The peak coupling efficiency occurs at $54.6\,m$, with a full-width half-max of $78\,m$. For this imaging skin, the maximum ratio of received power to total power from a point

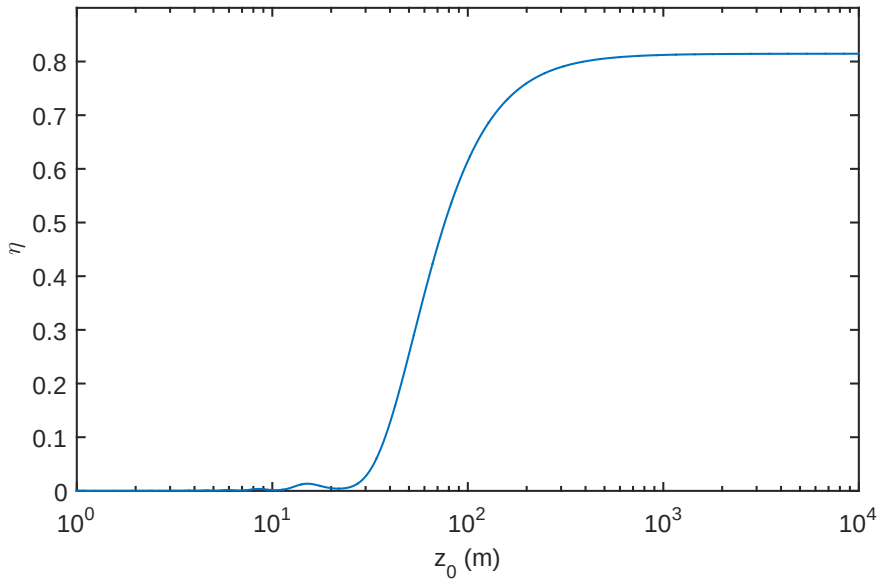

Figure 2.7: Efficiency of a point source as a function of distance

source is 8.259×10^{-10}, which is about 31% of the maximum for a refractive lens of the same area and distance. So long as z_0 is larger than the confocal parameter, the inverse square law dominates and the power received from a point is 82% the value for a similarly sized lens.

The previous analysis represents the maximum efficiency for a grating coupler with uniform coupling coefficient. Several loss mechanisms were not considered which could significantly decrease optical throughput. Common waveguide losses, such as material absorption and surface roughness scattering, are small for reasonable grating lengths and can be safely ignored. When the mode power is measured, there will be a reflection due to the index mismatch. Although this loss may be significant, it is not unique to this technique. These types of losses can accounted for by a simple multiplication with the efficiency found earlier.

There exists a loss mechanism which would necessitate a different form of analysis. If the substrate has a higher index than the superstrate, as has been assumed for this

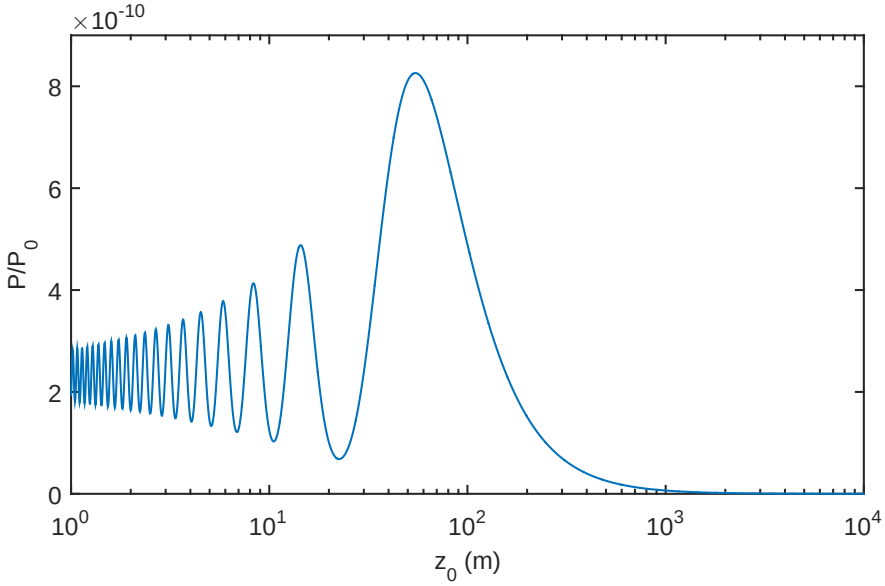

Figure 2.8: Power efficiency of a point

device, it is impossible to excite an unbound mode in the later without also exciting at least one in the former [14]. The radiating mode in the substrate adds an additional port so that reciprocity is no longer a sufficient condition for using the overlap integral. Instead, some coupled mode analysis is required to find the efficiency for a specific system. Because this form of analysis does not generalize well, it will be omitted.

2.3 Grating Design

The design parameters of an infinite conjugate imaging skin are shown in figure 2.9. As discussed in section 2.1, the grating length, L_g, is determined by the desired angular resolution. There are a variety of possible waveguide systems. Specifically, the thickness and material for the core and substrate are chosen to provide a desired mode profile. The superstrate will be assumed to be air to minimize system weight and ease fabrication. Once the mode's propagation constant is known, the grating period, d, is chosen so the

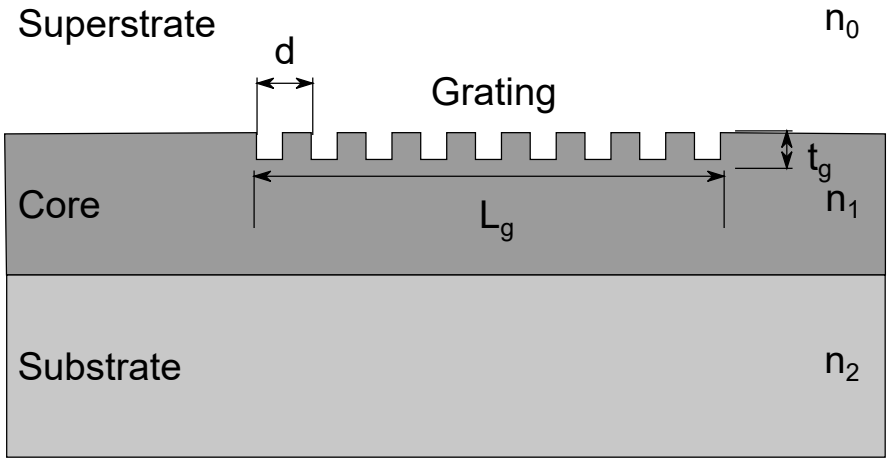

Figure 2.9: Illustration of grating design parameters

radiating mode out-couples at the desired angle, θ_0. Once all other parameters have been chosen, the grating depth, t_g is adjusted to obtain a desired coupling length. An example design follows where each stage is given in some detail.

There are many material systems which form planar waveguides. A common technique is to deposit dielectric films on a silicon wafer. These films must be very uniform as small perturbations result in large scattering losses [15]. To support a guided mode,

$$n_1 > n_2, n_0, \tag{2.15}$$

where n_0, n_1, and n_2 are the index of the superstrate, core, and substrate respectively. A symmetric waveguide, $n_0 = n_2$, can support at least one mode at every wavelength regardless of core thickness. When the guide is asymmetric, a mode is supported if and only if

$$V \geq \arctan\left[\frac{\sqrt{n_2^2 - n_0^2}}{\sqrt{n_1^2 - n_2^2}}\right], \tag{2.16}$$

where V is a normalized parameter given by

$$V = 2\pi \frac{t_{core}}{\lambda_0}\sqrt{n_1^2 - n_2^2} \tag{2.17}$$

If Eq. 2.15 is satisfied, the system will support a mode if the core is made thick enough. Specifically, the minimum core thickness is

$$t_{core} \geq \frac{\lambda_0}{2\pi\sqrt{n_1^2 - n_2^2}} \arctan\left[\frac{\sqrt{n_2^2 - n_0^2}}{\sqrt{n_1^2 - n_2^2}}\right]. \tag{2.18}$$

To make the system thin, the index of the core should be much larger than the index of the cladding layers.

If a single detector is used, the waveguide must also be single-mode. The modes of a planar guide are either the transverse electric (TE_v) or transverse magnetic (TM_v) modes, where v is a non-negative integer. The number of modes grows monotonically with the V number. The minimum V needed for the guide to support the v^{th} mode is [16]

$$V_{c,TE} = \arctan\left[\frac{\sqrt{n_2^2 - n_0^2}}{\sqrt{n_1^2 - n_2^2}}\right] + v\pi \tag{2.19}$$

for TE modes and

$$V_{c,TM} = \arctan\left[\frac{\left(n_1^2/n_0^2\right)\sqrt{n_2^2 - n_0^2}}{\sqrt{n_1^2 - n_2^2}}\right] + v\pi \tag{2.20}$$

for the TM modes. From Eqs. 2.19 and 2.20 the cutoff for the $v+1$ mode is always greater than the v mode. The one mode of a single-mode planar waveguide is always TE_0. For TE_1, and all higher TE modes to be cutoff

$$V < \arctan\left[\frac{\sqrt{n_2^2 - n_0^2}}{\sqrt{n_1^2 - n_2^2}}\right] + \pi \tag{2.21}$$

Likewise, if the TM_0 mode is cutoff, all transverse magnetic modes are also cutoff. The TM_0 cutoff condition is

$$V < \arctan\left[\frac{\left(n_1^2/n_0^2\right)\sqrt{n_2^2 - n_0^2}}{\sqrt{n_1^2 - n_2^2}}\right]. \tag{2.22}$$

For a given wavelength and set of materials, maximum core thickness is determined by the minimum of Eqs. 2.22 or 2.21.

The thickness of substrate and superstrate is less restrictive than the thickness of the core. To ensure that the finite width of the cladding layers does not effect the mode profile, those widths must be considerably larger than the decay length of their evanescent tail. Specifically, the substrate and superstrate must be thicker than

$$\gamma = \sqrt{\beta^2 - n_2^2 k^2} \tag{2.23}$$

and

$$\delta = \sqrt{\beta^2 - n_0^2 k^2} \tag{2.24}$$

respectively, where $k = 2\pi/\lambda_0$ and β is the mode propagation constant. In order for γ and δ to be purely real, meaning the mode does not propagate in these strata, $n_2 k \leq \beta$ and $n_0 k \leq \beta$. A similar condition can be derived by requiring transverse wave number in the core region,

$$\kappa = \sqrt{n_1^2 k^2 - \beta^2}. \tag{2.25}$$

be real. Assuming $n_2 \geq n_0$, the propagation constant is in the range $n_2 k \leq \beta \leq n_1 k$. Substituting the range of allowed β in Eqs. 2.23 and 2.24 yields

$$0 \leq \gamma \leq k\sqrt{n_1^2 - n_2^2} \tag{2.26}$$

$$k\sqrt{n_2^2 - n_1^2} \leq \delta \leq k\sqrt{n_1^2 - n_0^2} \tag{2.27}$$

A reasonable condition for the substrate thickness is $t_{sub} \geq 10k\sqrt{n_1^2 - n_2^2}$. The superstrate has a similar condition $t_{sup} \geq 10k\sqrt{n_1^2 - n_0^2}$. When the superstrate is air, this is a minimum distance within which other materials may be present. The value 10 was chosen such that the field strength decreases by $4.5 \times 10^{-3}\%$ the amplitude at the core-cladding interface. A higher value would further reduce the sensitivity of the mode profile to the environment.

The range of allowed propagation constants can be quite large, especially for high

contrast guides. To calculate the propagation constant precisely, one solves the characteristic equation

$$\tan(\kappa d) = \kappa \frac{\gamma + \delta}{\kappa^2 - \gamma\delta}, \tag{2.28}$$

for TE and

$$\tan(\kappa d) = n_1^2 \kappa \frac{n_0^2\gamma + n_2^2\delta}{n_2^2 n_0^2 \kappa^2 - n_1^4 \gamma\delta} \tag{2.29}$$

for TM modes. Both the left and right side of these equations are non-linear functions of β and cannot be solved analytically. Several numerical techniques have been developed for solving transcendental equations of this type including the Newton-Raphson and graphing methods. A final useful parameter is the effective index which is given by

$$n_{eff} = \frac{\beta}{k}. \tag{2.30}$$

Like the material refractive index, the effective index is equal to the ratio of the speed of light to the speed of the wave propagation in the guide. In the design of a grating coupler, the effective index is the only waveguide parameter needed to determine the out-coupling angle.

The material system chosen for the imaging experiments was a silicon nitride core deposited on a silica substrate. The superstrate was air. The index of PECVD Nitride is known to have large variations in index based on the growth conditions [17]. For the design example, an index $n_1 = 1.9$ is assumed. Substituting the indices of refraction and the design wavelength ($632.8\,nm$) in equations 2.18 and 2.22 yields the range of thickness for the nitride layer $59.08\,nm \leq t_{core} \leq 104.24\,nm$. A wafer with $t_{core} = 200\,nm$ was used instead because it was already available. At this thickness, the guide supports TM_0, but not the TE_1 or higher modes. Each modes' propagation constant and effective index are given in table 2.1.

The out-coupling angle, θ_0, has a range of acceptable angles. To get the maximum

Mode	$\beta(\mu m^{-1})$	n_{eff}
TE_0	16.704	1.6823
TM_0	15.659	1.5771

Table 2.1: Mode propagation constant and effective index for nitride guide ($\lambda = 632.8\,nm$)

angular resolution for a given grating length, the mode should exit normal to the waveguide surface. The out-couple angle is described by lateral phase matching condition [14]

$$n \sin\theta_0 = n_{eff} - q\frac{\lambda}{d} \tag{2.31}$$

where q is the diffraction order, and d is the grating period. The grating is assumed to not significantly change the mode structure, so n_{eff} is taken to be the same everywhere along the guide. Larger perturbations should be avoided because the mode mismatch causes a reflection at the interface.

The grating index has been assumed to be a periodic in position. Any periodic function can be expressed as

$$n(x) = \sum_{q=-\infty}^{\infty} c_q \exp\left[\frac{j2\pi qx}{d}\right], \tag{2.32}$$

where c_q is a complex constant given by

$$c_q = \frac{1}{d}\int_{-d/2}^{d/2} n(x) \exp\left[\frac{-j2\pi qx}{d}\right]. \tag{2.33}$$

Each Fouier component gives rise to a separate diffraction order [11]. If the grating index is a perfect sinusoid, all $c_q = 0$ except $q = -1$ and $q = 1$. In that case, the grating supports only the ± 1 diffraction orders. Even in the thin holographic gratings, there are some harmonic terms because the relationship between the refractive index and exposure intensity is not completely linear. It is straightforward to show that the

Fourier components for the binary relief grating are

$$c_q = \begin{cases} n_1 D + n_0(1-D), & q = 0 \\ \frac{(n_1 - n_0)}{D} \mathrm{sinc}\left(qD\right), & q \neq 0 \end{cases} \tag{2.34}$$

where D is the square wave duty cycle. To maximize the first diffraction order, the duty cycle is 50%.

The range of allowed grating period d, is set by the requirement that there be one and only one diffraction order in the superstrate. Multiple diffraction orders would result in ambiguity. Specifically, the detected power would consist of an unknown mixture of the different orders. According to Eq. 4.2, the condition for the first diffraction order to exist is

$$-1 < n_{eff} - \frac{\lambda}{d} < 1, \tag{2.35}$$

because the sine function has a range of ± 1. If the second diffraction order is cutoff, so too are the higher orders. The cutoff condition for the second order is

$$n_{eff} - 2\frac{\lambda}{d} < -1. \tag{2.36}$$

To keep coupling efficiency high, a designer should minimize the number of modes which radiate into the substrate. Because the substrate has a higher index than free space, it is not possible to have a superstrate order without exciting at least one in the substrate. The second substrate order is cutoff when

$$\frac{1}{n_2}\left(n_{eff} - 2\frac{\lambda}{d}\right) < -1. \tag{2.37}$$

Plotting these inequalities, as shown in Fig. 2.10, allows a designer to quickly identify the range of allowed grating periods for a given effective index. The regions where the modes are forward ($\theta > 0$) or backward scattering ($\theta < 0$) have been separated to easily tell where $\theta = 0$.

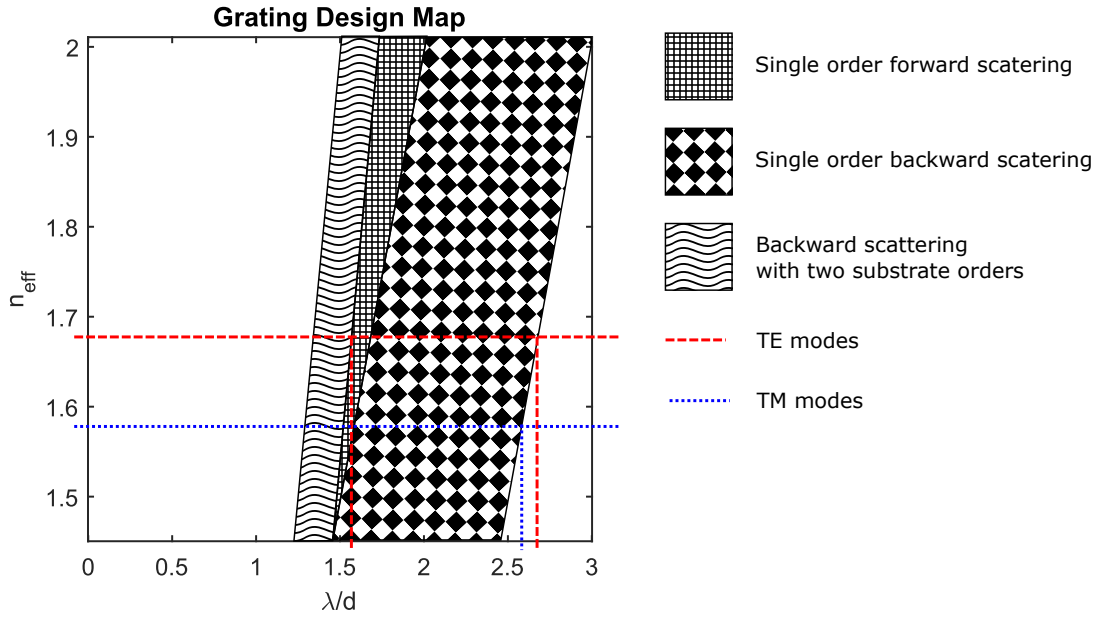

Figure 2.10: Grating design window with modes of nitride guide at 632.8 nm

The design inequalities for the nitride guide are shown in figure 2.10. The calculated effective index for each mode has been indicated by horizontal lines. The range of λ/d, determined by the intersection of the n_{eff} line and the single order region boundaries, is $1.39 \leq \frac{\lambda}{d} \leq 2.68$. For $\lambda = 632.8nm$, the range of allowed period is

$$236.1\,nm \leq d \leq 472.2\,nm \tag{2.38}$$

To ensure there is only one substrate order, $d \leq 404.1\,nm$. The actual grating period was $460\,nm$, therefore this particular imaging skin is not as efficient as it could be.

Once the waveguide and grating period have been set, one can find the grating depth, t_g which gives the coupling length equal to the grating length. There is no analytic equation which describes this relationship. Many methods, however, have been developed including coupled mode theory [16], a transmission line model [14], volume current method [18], and iterative approaches such as those proposed in [19]. In this case, the coupling length for different grating depths was calculated using the boundary

element method [20]. The plot of this simulation is shown in Fig. 2.11. For a $1 \pm 0.2\,cm$ coupling length, we need an etch depth of $4 \pm 0.5nm$. Because the etch depth is so shallow, the simplest perturbation techniques should have sufficient accuracy and do agree with the boundary element analysis.

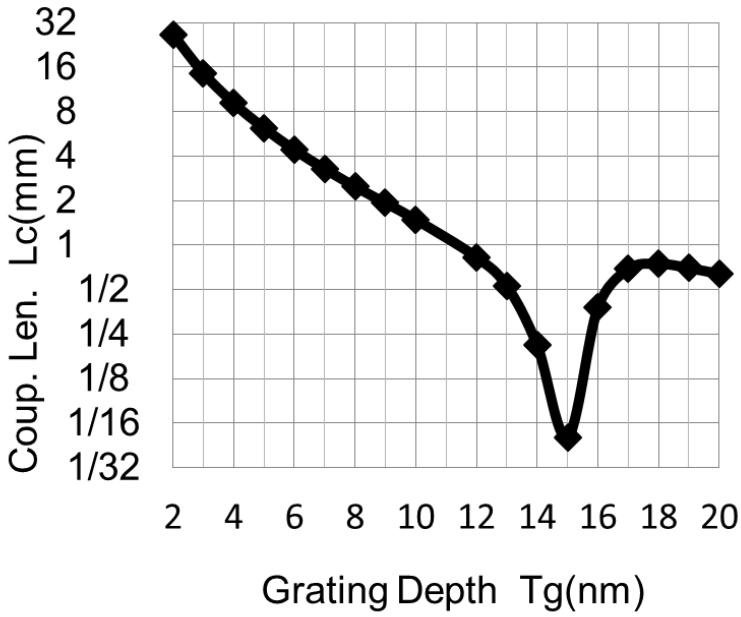

Figure 2.11: Grating length calculated for different grating depths using the boundary element method

The design of an imaging skin begins by choosing the waveguide materials and material thicknesses. After the modes' effective index has been calculated, a grating period is calculated for a desired out-coupling angle. Finally, the grating depth is determined for a given coupling length. It is possible that at the end of this design procedure, the device is not fabricatable. Specifically, the grating pitch (d) or depth (t_g) might be smaller than the available process resolution. One can increase t_g while keeping L_c constant if a material with lower index contrast is used. From Fig. 2.10, a larger period can be used to obtain the same output angle if the effective index is decreased. This can be accomplished by using a thinner core. The prescribed procedure

did yield a workable design for a grating coupler based imaging skin.

2.4 Grating Fabrication

A surface relief grating is fabricated in two steps. First the pattern is written in photoresist using interference lithography. After the resist is developed, the pattern is transferred into the nitride material by wet etching. Both techniques are reviewed, but details will focus on the specific device under investigation.

Several techniques are available for writing a pattern on a planar surface. Laser writers and optical contact lithography do no have sufficient resolution for the designed grating period. Optical projection and electron beam lithography are capable of producing the requisite line widths, but these systems were prohibitively expensive. One of the first techniques used for creating grating couplers was interference lithography.

The exposure setup used to write the gratings is shown in Fig. 2.12. An argon ion laser was chosen based on the availability of a strong UV line and very good spatial mode profile. The light is divided in two by the beam splitter (BS). Each arm is expanded by a spatial filter (SF) and collimated with a $50\,cm$ focal length lens. The interference of two plane waves forms a periodic pattern in intensity. The waveguide is oriented so its surface normal bisects the angle between the two plane waves. Given the amplitudes of the two beams are A_1 and A_2, the intensity at the surface is

$$I = A_1^2 + A_2^2 + 2A_1A_2 \cos\left[\frac{4\pi}{\lambda}\sin(\theta/2)x\right] \tag{2.39}$$

where θ is the angle between the two plane waves. A variable neutral density filter (ND) is inserted in one arm to balance the beams intensity, $|A_1|^2 = |A_2|^2$, maximizing the fringe visibility.

The period of the grating is determined by the choice of angle between the two

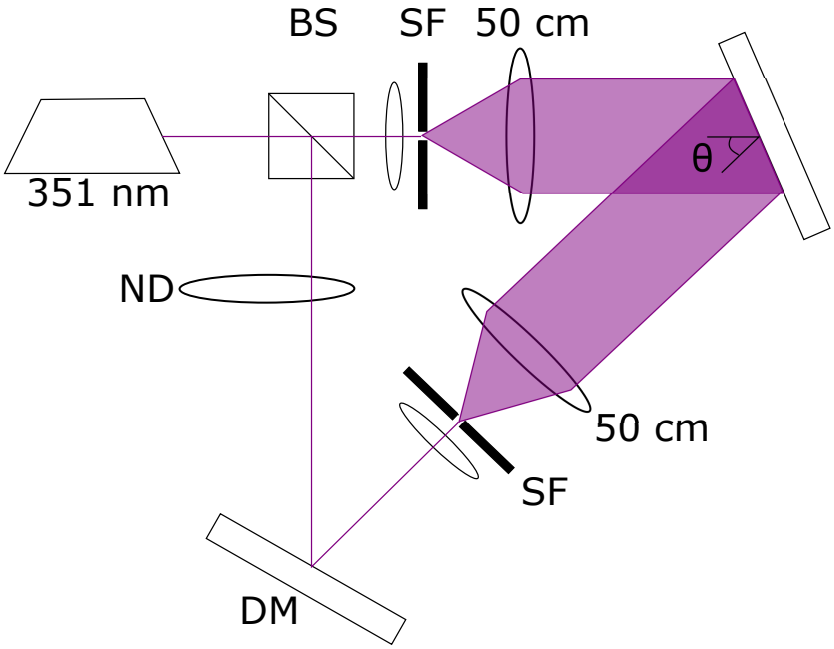

Figure 2.12: Interference lithography setup

beams. Specifically, the period of the cosine term in Eq. 2.39 is

$$d = \frac{\lambda}{2\sin\left(\frac{\theta}{2}\right)}. \tag{2.40}$$

This relation, assuming a wavelength of $351nm$, is plotted in Fig. 2.13. As the beams approach parallel, $\theta \to 0$, the grating period approaches infinity. The minimum period, $d = \lambda/2$, occurs when the beams are anti-parallel ($\theta = 180°$).

While it is possible to make any period in the range $\lambda/2 \leq d \leq \infty$, a designer should keep in mind the sensitivity of the period to angle mismatch. In addition to simple alignment error, a small phase curvature in one or both beams can result in a significant chirp in the grating period. This sensitivity is given by the derivative of Eq. 2.40, which is

$$\frac{\partial d}{\partial \theta} = \frac{\lambda}{2}\frac{\cos\theta/2}{\cos\theta - 1}. \tag{2.41}$$

The grating period is least sensitive to perturbations in θ when beams are anti-parallel,

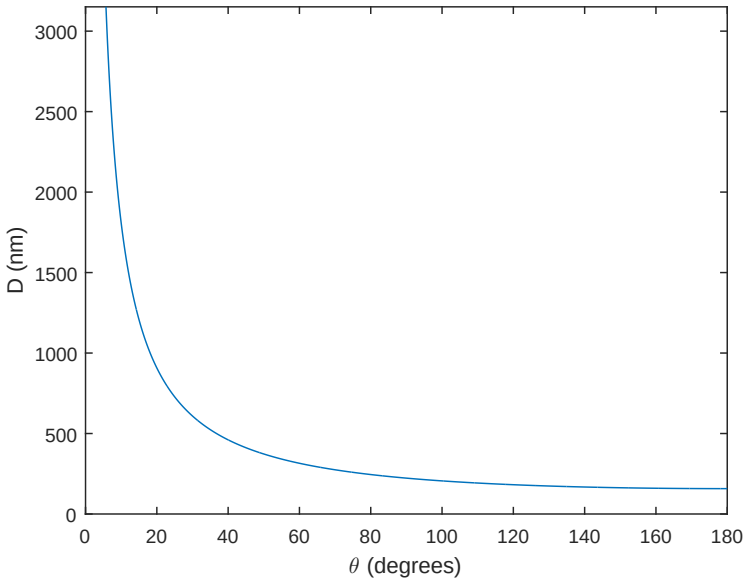

Figure 2.13: Period vs angle for $\lambda = 351nm$

or $d = \lambda/2$. As long as the two beams are at oblique angles, $|\frac{\partial d}{\partial \theta}| \leq \lambda\sqrt{2}/2$. Restricting the range of angles to $\pi/2 \leq \theta \leq \pi$, the range of possible grating periods is narrowed to

$$\frac{\lambda}{2} \leq d \leq \frac{\lambda\sqrt{2}}{2}. \tag{2.42}$$

While the maximum period is a soft criteria, the minimum period is a physical hard limit.

Let us return to the fabrication of the grating designed in section 2.3. Solving Eq. 2.40 for θ yields the design equation

$$\theta = 2\sin^{-1}\left(\frac{\lambda}{2d}\right). \tag{2.43}$$

Substituting $\lambda = 351\,nm$ and the range of the allowed periods from Eq. 2.38, Eq. 2.43 yields an allowed angle range of $43.64° \leq \theta \leq 96.03°$. The $460\,nm$ grating was written by setting $\theta = 44.86°$. The concern for misalignment tolerance mentioned previously, is

evident in this example. If the angle between the two beams is off by 1.2°, the guide will have multiple diffraction orders in the air and will not be usable as an imaging skin.

Once the pattern has been written, there are two options. The patterned photoresist layer itself can act as the grating [8]. The pattern, in our experiments, was transferred into the silicon nitride by etching to increase device longevity. Several methods exist for etching, but they can be roughly divided into two classes: wet and dry etching. Dry etching typically has a higher degree of anisotropy; wet etches offer better chemical specificity [21]. Because the etch depth was far less than the lateral feature size, anisotropy was not a large concern and wet etch was selected.

Etch rates for PECVD nitride vary widely, $1500 - 3000\,A/min$, depending upon the density of the material [22]. A step etch was used to find the concentration of etchant and approximate etch timing. It was found that a 1:100 concentration of buffered oxide etch in deionized water yielded a $5\,nm$ etch after $10\,s$. The etch depth was measured using an atomic force microscope, AFM, a small section of which is shown in Fig. 2.14. A slice taken perpendicular to the grating direction, as plotted in 2.14**(b)**, shows the etch depth was approximately $5\,nm$.

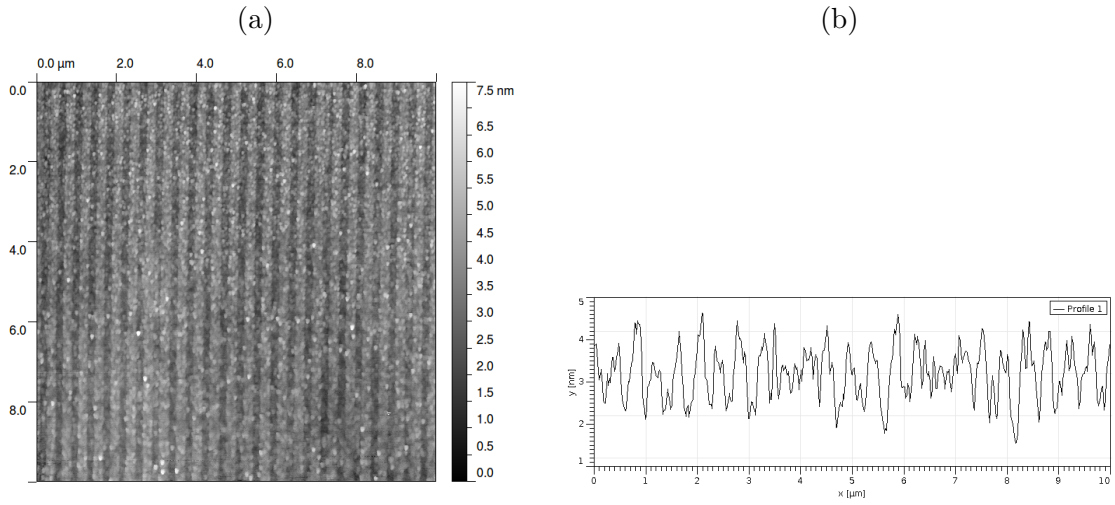

Figure 2.14: (a) AFM of grating coupler and (b) horizontal slice through AFM data

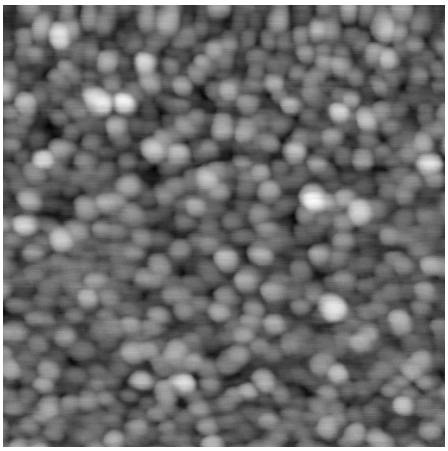

Figure 2.15: AFM of un-patterned nitride

The slice in Fig. 2.14 b also shows that there was significant surface roughness after the etch. Similar surface roughness is observable in the nitride before etching as shown in 2.15. Even before patterning, the RMS height of this material is $2.3\,nm$. Surface roughness, in this case, becomes the limiting factor on coupling length, and ultimately, imaging resolution. By changing to a lower index contrast, one could increase the grating depth needed to obtain a certain coupling length. Reducing the index contrast, however, would necessitate using a thicker core. A better solution may be to perform chemical mechanical polishing (CMP) which has been shown to produce near atomic flatness. Polishing would be completely ineffective, however, if the material itself is porous. Generally, the higher the desired resolution, the higher quality the requisite films.

2.5 Angle Spread Function When Using a Point Detector

In the previous sections, it has been assumed that the guided mode only propagates in the x-direction. While it is possible to isolate this component using additional optics, a simple point detector will measure power over a continuum of angles. Using reciprocity,

the angle spread function is calculated by tracing rays from a point source through the grating and into the far-field.

By fabricating the waveguide in a dielectric stack on a silicon wafer, the detector can be fully integrated [23]. The detection system used in these early experiments, which is functionally equivalent to an integrated point detector, is shown in Fig. 2.16. A point on the waveguide end-facet is imaged by a microscope objective onto a bulk detector. The numerical aperture of the objective is larger than the NA of light exiting the guide. Therefore, the in-plane angle spread (ψ_{max}) is determined by the width of the grating (L_g, y) and the distance from the grating to the end-facet (L).

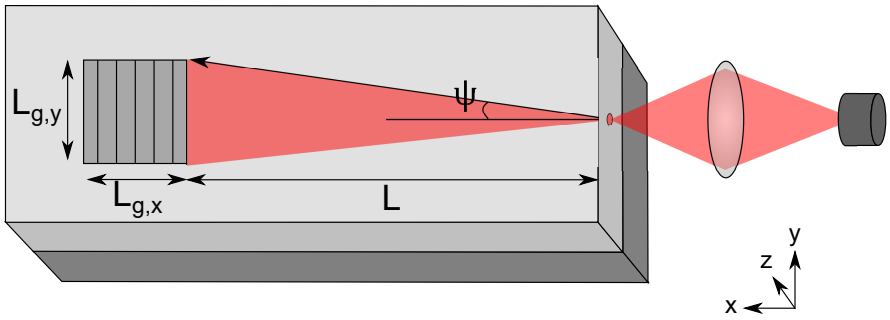

Figure 2.16: Illustration of a detection system for an imaging skin

According to [24], the direction vector of a first-order out-coupled ray from a grating coupler is

$$\begin{aligned}\vec{S}_0 &= \hat{x}\left(n_1 \cos\psi \sin\alpha - \frac{\lambda}{d}\right) \\ &+ \hat{y}\left(n_1 \sin\psi \cos\alpha\right) \\ &+ \hat{z}\sqrt{n_1^2 \cos^2\alpha - \left[n_1^2 - n_0^2 + \left(\frac{\lambda}{d}\right)^2 - \frac{2\lambda n_1}{d}\cos\psi \sin\alpha\right]},\end{aligned} \tag{2.44}$$

when the incoming ray direction ($\vec{S}_G$) is

$$\vec{S}_G = (\cos\psi \sin\alpha)\,\hat{x} + (\sin\psi \sin\alpha)\,\hat{y} + (\cos\alpha)\,\hat{z}. \tag{2.45}$$

As before, λ is the free space wavelength, d is the grating period and n_0 and n_1 are index of refraction for the superstrate and core respectively. The inclination angle α is a constant given by

$$\alpha = \arcsin\left(\frac{\beta\lambda}{2\pi n_1}\right), \tag{2.46}$$

where β is the mode propagation constant. The in-plane angle ψ is position dependent as described by

$$\psi = \arctan\left(\frac{y}{x + Lg/2 + L}\right). \tag{2.47}$$

Like in other ray-tracing, the grating area is discretized and the ray direction is calculated at each point. The angles of the ray with respect to the surface normal, for $L = 1$, 2, 3, 4, and $5, cm$, are shown in Fig. 2.17. For all lengths, the curve in angle space has the same shape but different extent. Specifically, the shorter length L, the longer the angle spread in the y-direction. The curve approaches a delta function as L goes to infinity.

Using a point detector, instead of assuming a plane wave, the ASF is spread over a sizable curve. Ray tracing does not include diffraction effects, but the width of the curve is inversely proportional to the grating length as described in section 2.1. An alternative design, where a point in space is mapped to a point in the waveguide, is presented in Ch. 6. To use the current design, the detector should be moved as far away from the grating as possible.

2.6 Experiments

After fabricating the grating-coupler, its angle spread function was measured using the setup shown in Fig. 2.18. A HeNe laser beam was expanded to approximately $32\,mm$ and was collimated by a $10\,cm$ lens. The power was measured, as described in section 2.5, by imaging the end facet of the waveguide while the device, objective, and CCD were

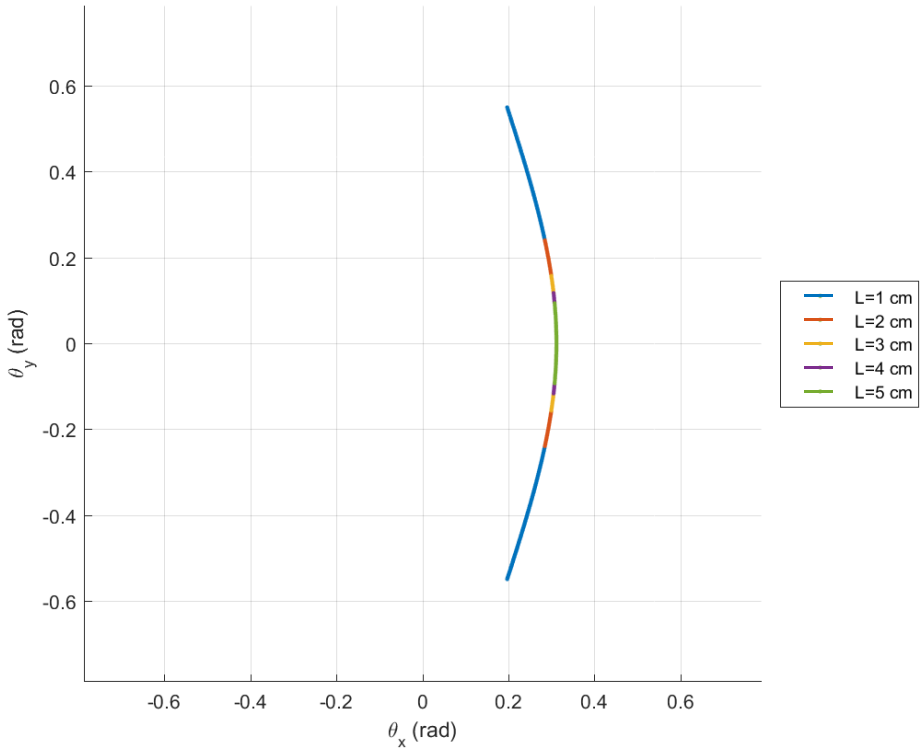

Figure 2.17: Simulated ASF for an imaging skin with a point detector

rotated on a single stage. The usage of a CCD, compared to a discrete detector, reduced the available dynamic range, but allowed for a drastic reduction in the measurement of scattered light. The measured power and Eq. 2.5 where $L_c = 4.4\,mm$ are shown in Fig. 2.19. The apparent coupling length was slightly smaller than the design. This was likely due to losses such as the second substrate mode and scatter from surface roughness.

As a proof of concept, an image was made of a pseudo-random barcode cutout of cardboard. The setup is shown in Fig. 2.20 was similar to the previous experiment. Instead of scanning by rotating the physical system, the object was translated in the front focal plane of a $10\,cm$ lens. To mitigate the effects of the curved ASF, the barcode

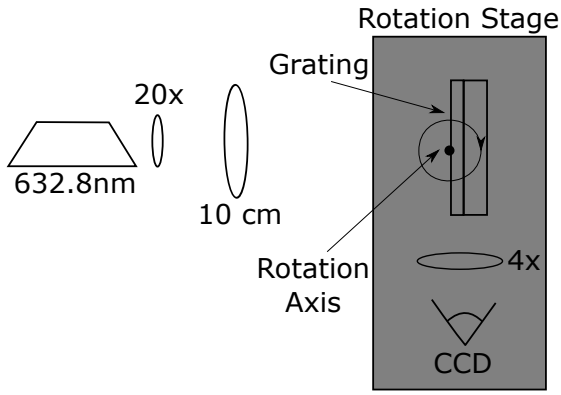

Figure 2.18: Experimental setup to measure the angle spread function of the imaging skin

was very narrow in the y-direction.

The captured image is compared to the original barcode in Fig. 2.21. Though the scan was one dimensional, the data is represented as a a 2D image. Some roll-off is observable close to the transitions resulting from the finite resolution of the system. The scanning was stopped before the end of the barcode resulting a missing bright bar at the far right. Overall, the image is a very good match to the original.

2.7 Conclusions

An imaging system using a grating coupler on a planar waveguide has been demonstrated. A procedure for designing a low-loss, high resolution infinite conjugate system was presented. Though surface roughness was a concern, the suggested fabrication technique produced a grating of a reasonable quality. While the active parts of the system were only a few wavelengths thick, the resolution was shown to be commensurate with the diffraction limit of a similarly sized lens. Using a single point detector, instead of isolating the guided mode propagating in the x-direction, results in severe reduction of resolution in the y-direction. Because it captures a single point at a time, an imaging

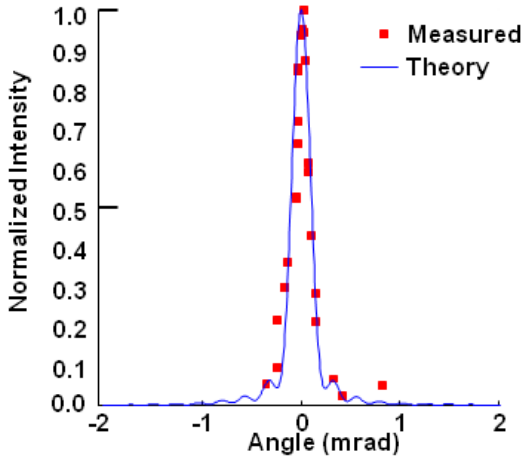

Figure 2.19: Measured angle spread function of imaging skin

skin must scan over the object. All scanned systems have significantly lower frame rates compared to a lens which captures all points in parallel. By making an image of a one-dimensional pseudo-random barcode, it has been shown that a high resolution imaging system can nearly be confined to a plane.

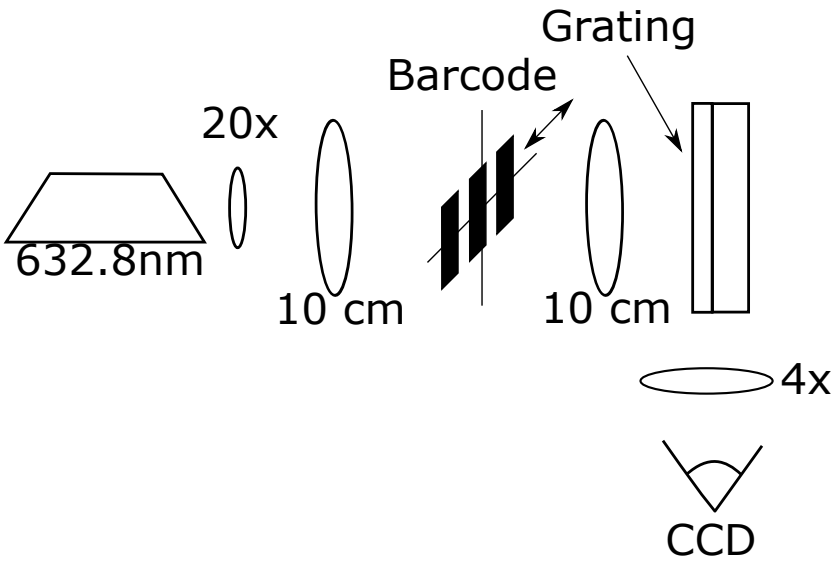

Figure 2.20: Image experimental setup

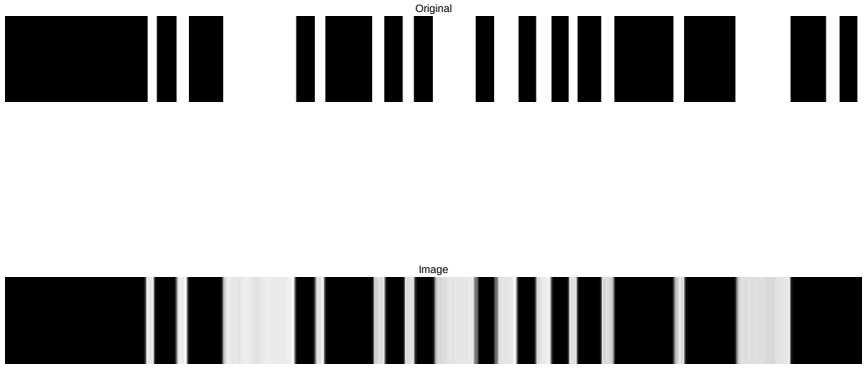

Figure 2.21: Imaging skin image of pseudo-random barcode

Chapter 3

Imaging Threads

The diffraction limit of an imaging system is inversely proportional to the extent of the system's aperture. If the pupil function is separable, that is it can be written in the form $p(x, y) = h(x) \times g(y)$, the resolution in the x-direction is independent of the resolution in the y-direction. If high resolution is required in a single spatial dimension, the aperture width in the orthogonal direction may be arbitrarily small. An imaging thread represents the extreme case where the entire imaging system is confined to a nearly one-dimensional form factor.

Imaging threads have several benefits over their two-dimensional counter parts. The one-dimensional form factor is particularly useful in applications, such as aerospace and surveillance, where weight and cross-sectional area have a high cost. Imaging threads are also simpler to implement. Commercially available connectors allow the system to integrate with premade detectors. In all imaging systems, bending from mechanical and thermal stresses are detrimental to system performance. The imaging skin mitigated this effect by supporting the waveguide with a rigid, relatively thick, silicon substrate. A thread-like system can accomplish the same effect simply by stretching the fiber between two points. Given these benefits, it is reasonable to ask if a high resolution imaging

system can be confined to a one-dimensional form factor.

In this work, only imaging threads which use a waveguide and grating coupler are considered. Specifically, the system consists of a tilted fiber Bragg grating (TFBG) on a single-mode optical fiber. These gratings are commonly fabricated by holographically exposing the gemanosilicate fiber core with a spatially periodic UV field [25]. TFBGs have been employed to measure acceleration, temperature, strain, pressure, refractive index, and biological/chemical concentrations [26]. For imaging applications, the TFBG is a convenient method to map a well-defined field in the object plane into a waveguide mode. An illustration of the proposed system is shown in Fig. 3.1. Consider a mode traversing the fiber. When the wave reaches the grating, power is out-coupled into a continuum of radiation modes. Using reciprocity, the same radiation pattern, but with conjugate phase, will excite the same mode in the fiber. The guided mode then propagates to a detector. To build up an image, the system scans over the object plane, most likely by physically rotating the fiber. Although the illustration shows a finite conjugate system, this chapter will be restricted to the infinite conjugates.

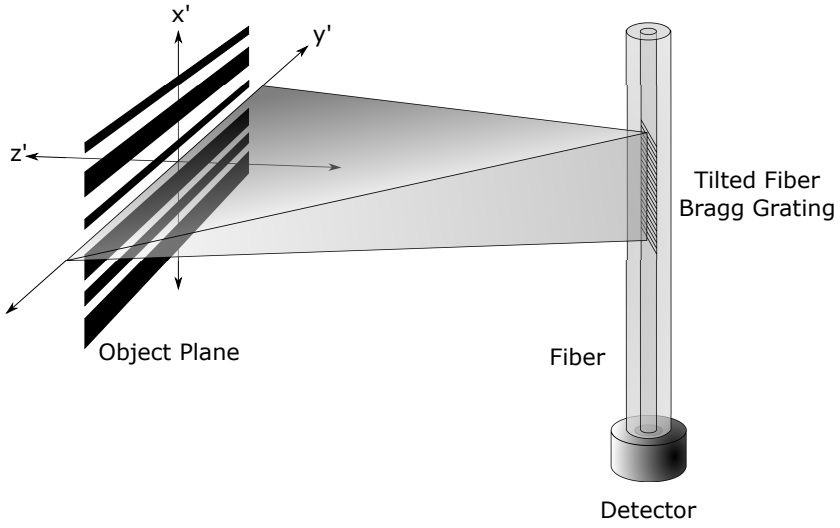

Figure 3.1: Illustration of a TFBG based imaging thread

There are many existing imaging systems that use optical fibers. These include conventional endoscopy, lensless systems [27], [28], and optical coherence tomography [29]. By adapting super-resolution techniques, such as STED [30] and two-photon fluorescence [31], fiber systems have even been able to exceed their diffraction limits. All of these systems can be classified as optical probes where the fiber serves as a conduit from a location with limited accessibility to a remote system for further processing. In these technologies, high spatial resolution is only possible if the fiber end-facet or lens assembly are in close proximity to the object. For the proposed technique, we are interested imaging at large object distances. By using the length of the fiber instead of the end-facet as the pupil, the proposed system can have much higher far-field resolution, albeit in a single spatial dimension.

3.1 TFBG Far-field Radiation Pattern

The point spread function completely describes the performance of an imaging system within the Fourier optic framework. By reciprocity, the PSF is equal to complex conjugate of the radiation pattern from an out-coupled mode. The PSF for the imaging thread is calculated in two stages. First, the locus of intersections between the out-coupling rays and the object plane is determined. In the next section, the width of the resulting curve is calculated using Fourier analysis.

It is convenient to use cylindrical coordinates when ray tracing the out-coupled mode from the TFBG. The longitudinal component of the wavevector, k_z, is given by the phase matching condition

$$k_z = \beta - q\frac{2\pi}{\Lambda_g}\cos\theta_g, \tag{3.1}$$

where β is the mode propagation constant, Λ_g is the grating period, θ_g is the grating tilt angle, and q is the diffraction order. Because the total momentum must be conserved,

the radial component of the wavevector is

$$k_r = \sqrt{\left(\frac{2\pi}{\lambda_0}\right)^2 n_0^2 - k_z^2}, \tag{3.2}$$

where n_0 is the surrounding index of refraction, which will be assumed to be unity. For each azimuthal angle ϕ, k_r and k_z are constants, therefore the radiation pattern moves away from the grating along the edge of a cone as shown in Fig. 3.2. The cone divergence angle θ_c, measured with respect to the fiber axis, is

$$\theta_c = \arctan\left(\frac{k_r}{k_z}\right). \tag{3.3}$$

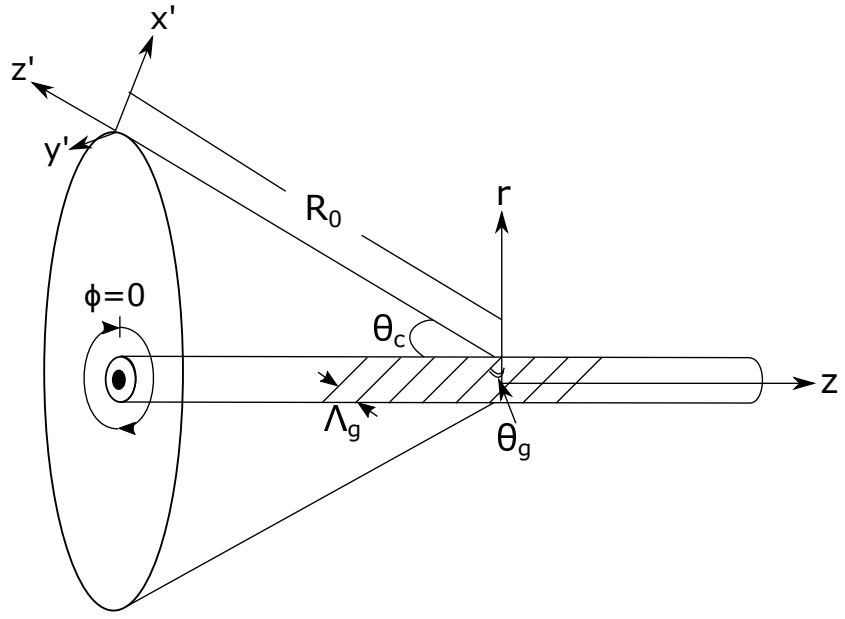

Figure 3.2: Out-coupled radiation modes propagate along the edge of a cone

To describe the TFBG as an imaging system, the imaging axis and object plane must be specified. The ray along the cone with maximum power, $\phi = 0$, is chosen to be the imaging axis and is indicated by z'. The object plane is normal to the imaging axis and a distance R_0 from the center of the grating. The object plane directions x' and y' correspond to infinitesimal changes in θ_c and ϕ respectively at the origin. The locus of

the intersections with the cone and the object plane, after some simplification shown in appendix B, is given by the parametric equations

$$x'(\phi) = \frac{R_0}{2}\frac{\sin 2\theta_c(\cos\phi - 1)}{\cos^2\theta_c + \cos\phi\sin^2\theta_c} \tag{3.4}$$

$$y'(\phi) = R_0\frac{\sin\phi\sin\theta_c}{\cos^2\theta_c + \cos\phi\sin^2\theta_c}. \tag{3.5}$$

The distance from the grating to each of these points is also a function of the azimuthal angle. As a result, the relative phase is given by

$$\psi(\phi) = \frac{2\pi}{\lambda}\left[R(\phi) - R_0\right] \tag{3.6}$$

$$= \frac{4\pi R_0}{\lambda}\frac{\sin^2\left(\frac{\phi}{2}\right)\sin^2(\theta)}{\cos(\phi)\sin^2(\theta) + \cos^2(\theta)}. \tag{3.7}$$

The phase of a PSF is unimportant when the object is spatially incoherent, but is critical for coherent imaging.

The positions of the radiation pattern was confirmed experimentally for a particular fiber (CorActive UVS-652) and grating. The propagation constant (β) for the LP_{01} mode is calculated by solving the characteristic equation

$$\frac{uJ_{-1}(ua)}{J_0(ua)} + \frac{wK_{-1}(wa)}{K_0(wa)} = 0, \tag{3.8}$$

where a is the core radius, and J and K are the Bessel functions of the first and second kind [32]. The normalized parameters u and w are given by

$$u^2 = n_1^2k^2 - \beta^2 \tag{3.9}$$

$$w^2 = \beta^2 - n_2^2k^2, \tag{3.10}$$

where n_1 and n_2 are the core and cladding indexes respectively and $k = 2\pi/\lambda$. The grating period and tilt angle were $1112.03\,nm$ and $30°$. For $\lambda = 1.3\,\mu m$, the 2nd diffraction order was the closest to Bragg matched with $\theta_c = 31°$. While q is typically assumed to be unity, higher diffraction orders have been observed [33]. These diffraction

orders have lower coupling efficiency, but the gratings which produce them have longer periods and are therefore typically easier to fabricate. The positions given in Eqs. 3.4 and 3.5, shown in Fig. 3.3 b, were confirmed by placing a CCD in the back focal plane of a $10\,cm$ lens, as shown in Fig. 3.3 **a**. The two curves agreed to such a high degree that plotting them on the same figure resulted in one occluding the other.

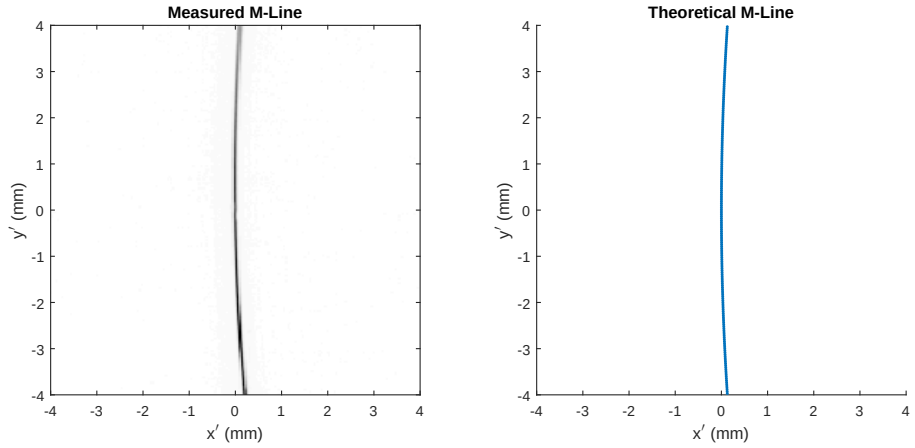

Figure 3.3: Radiation pattern in the far-field **(a) measured (b) theory**

If the grating planes are perpendicular to the z-axis, the system is circularly symmetric and the power is uniformly distributed in ϕ. This configuration, however, cannot efficiently couple light into free space. The tilt in the fiber grating allows a radiation mode to be Bragg matched, but also breaks the rotational symmetry. The distribution over ϕ, whch determines the resolution in the y-direction, has been calculated by coupled mode theory [34] and the Volume Current Method [35]. From the later, the Poynting vector for light exiting a TFBG is

$$\begin{aligned}\vec{S} &= \frac{\pi k_0^2 c\kappa^2 E_0^2}{4\epsilon_0 \cdot r}\left(\frac{k_z^2}{k_0^2 n_1^2}+\frac{k_t^2}{k_0^2 n_1^2}\sin^2(\delta-\phi)\right)\\ &\times \left[\frac{K_{new}aJ_0(ua)J_1(K_{new}a)-uaJ_1(ua)J_0(K_{new}a)}{K_{new}^2-u^2}\right]^2\left(\hat{r}+\frac{k_z}{k_t}\hat{z}\right), \quad (3.11)\end{aligned}$$

where κ is proportional to the grating index modulation amplitude, E_0 and δ are the

amplitude and polarization angle of the fiber mode, and a is the fiber radius. k_t is similar to k_r except inside the core and is given by

$$k_t = \sqrt{n_1^2 k^2 - k_z^2}. \tag{3.12}$$

$\vec{K}_{new}$ is the lateral wavevector mismatch given by

$$\vec{K}_{new} = -\frac{2\pi}{\Lambda_g} \sin\theta_g \hat{x} + \hat{k}_t. \tag{3.13}$$

From 3.11, the distribution of power over the azimuthal angle is primarily determined by K_{new}. If K_t and k_t are both large and have comparable magnitude, the dependence on ϕ becomes large. When $\theta_g = 45°$, the extent of the radiation in the azimuthal direction is minimized. This tilt angle also results in a Bragg angle of $\theta_c = \pi/2$. Instead of an ellipse, the locus of rays fall on a line in the y'-direction, and the length of that segment is at a minimum with respect to θ_g. Therefore, TFBGs for imaging threads should be designed for normal incidence whenever possible.

3.2 Imaging Thread Resolution

The amplitude (Eq. 3.11), phase (Eq. 3.7) and position (Eqs. 3.4, 3.5) determine all aspects of the imaging thread PSF except its width. In the previous discussion, the cone angle was taken to be a single value. Because any real grating is finite in extent, θ_c, has some width due to diffraction. It is this angle spread which determines the resolution of the system in the dimension of interest. The angle spread function for a particular grating is calculated and confirmed through direct measurement.

The resolution of imaging thread in the x'-direction can be calculated by an analysis similar to the one given in section 2.1. The out-coupled field, just outside the grating, for the imaging thread is given by

$$A(z) = A_0 \exp\left[-\frac{z + L_g \sin\theta_c/2}{L_c \sin\theta_c}\right] \times rect\left[\frac{z}{L_g \sin\theta_c}\right]. \tag{3.14}$$

This expression is equivalent to Eq. 2.4 except the $\sin\theta_c$ term was used in place of $\cos\theta$ because θ_c is referenced to the fiber's propagation direction instead of its normal. The far-field pattern is obtained by taking a Fourier transform and substituting the Fourier conjugate variable for $\theta_{x'}/\lambda$. Under the small angle approximation, the radiation pattern is

$$\mathcal{A}(\theta_{x'}) = \frac{2\exp\left(\frac{-L_g}{2L_c}\right)\sinh\left(\frac{-L_g}{2L_c} + \frac{i\pi L_g \sin\theta_c}{\lambda}\theta_{x'}\right)}{\frac{1}{L_c\sin\theta_c} + \frac{i2\pi}{\lambda}\theta_{x'}}, \tag{3.15}$$

where λ is the wavelength. Like the imaging skin, the resolution is proportional to the smaller of L_g or L_c.

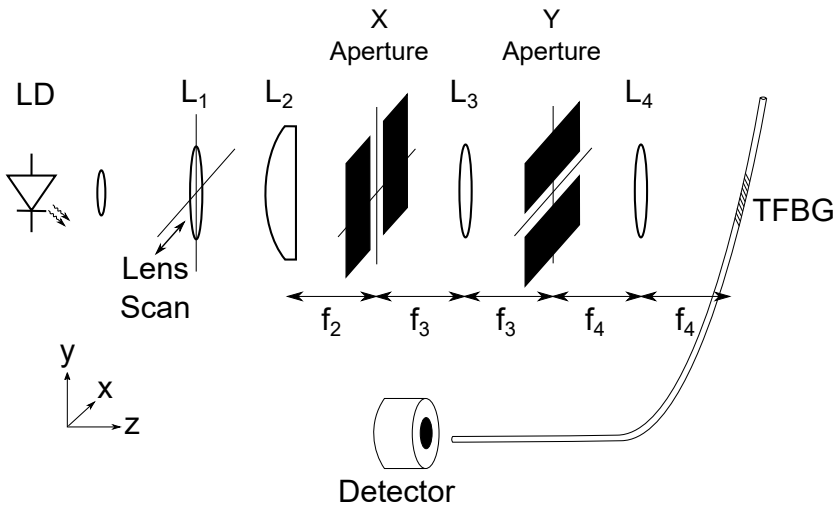

Figure 3.4: Setup for measuring the angle spread function

To validate Eq. 3.15, the angle spread function was measured using the system shown in Fig. 3.4. The beam from a 1.3 μm laser diode, LD, was collimated by a 10 cm focal length spherical lens (L_1). This beam was focused down to a line by cylindrical lens (L_2). An afocal system (L_3 and L_4) with unity magnification projected the apertured line onto the fiber. To mitigate the effects from the PSF curvature (resulting from $\theta_c \neq \frac{\pi}{2}$ in our experiment), the beam was apertured in the y-direction in the afocal

system's Fourier plane. Finally, a detector measured the power exiting the fiber's end-facet. The angle scanning was performed by translating L_1 rather than rotating the fiber. For small angles, the two scanning methods are equivalent.

The normalized measured power with respect to angle ($\theta_{x'}$) is shown in figure 3.5 a for an x aperture set to 1, 2, and 4 mm. Because of the 31° projection angle, the external apertures correspond to approximately 2, 4, and 8 mm at the fiber surface. The normalized square-magnitude of Eq. 3.15 with a coupling length $L_c = 6$ mm, and the same grating lengths are shown in figure 3.5 b. The two sets of curves are in good agreement for all aperture widths. The measurement was repeated with no external aperture and is consistent with a grating width of 11 mm. Because the exact grating length was not known, a corresponding theoretical curve was not calculated. While the exact cause of the asymmetry in the 8 mm and no aperture curves is yet unknown, it is likely a consequence of the scanning technique rather than a feature of the grating. As predicted, the width of the angle spread function goes as the inverse of grating length.

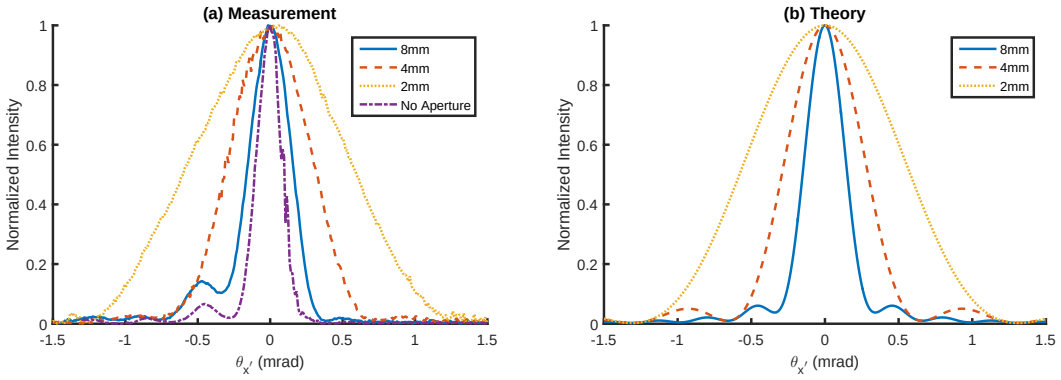

Figure 3.5: Comparison of the measured (a) and theoretical (b) angular spread functions for varying aperture widths

3.3 Imaging Example

Adding a chirp to the grating period or a physical curve in the fiber can focus the light out-coupling from the grating to a plane a finite distance away. This would correspond to traditional finite conjugate imaging. The simple TFBG, however, maps a fiber mode to the point spread function in the far field. To test the imaging performance of our infinite conjugate system, an optical projection system was designed to simulate a set of object points at an infinite distance from the fiber. This setup is shown in figure 3.6.

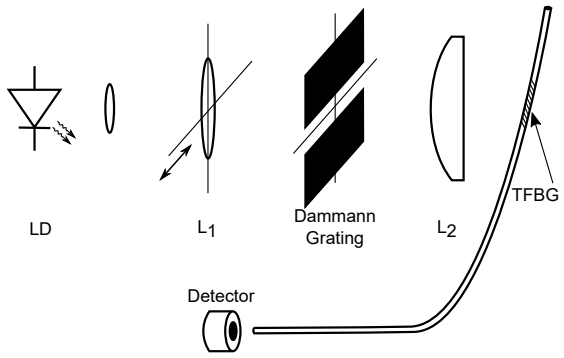

Figure 3.6: Imaging setup

A Dammann grating, designed to produce six, equal weight diffraction orders, was illuminated with a collimated 1.3 μm laser diode (LD). Each diffraction order of the Dammann grating simulates a distinct point at infinity without needing a Fourier transforming lens. To increase coupling efficiency, a cylindrical lens (L_2) focused the expanded beam onto the fiber. This lens had no focusing power in the imaging direction, but did allow for phase matching in the transverse direction. Translating the collimating lens scanned the angle without moving the object nor the imaging thread. In practice, scanning is likely to be accomplished by physically rotating the fiber.

An independent measurement of the object intensity pattern, captured by a CCD

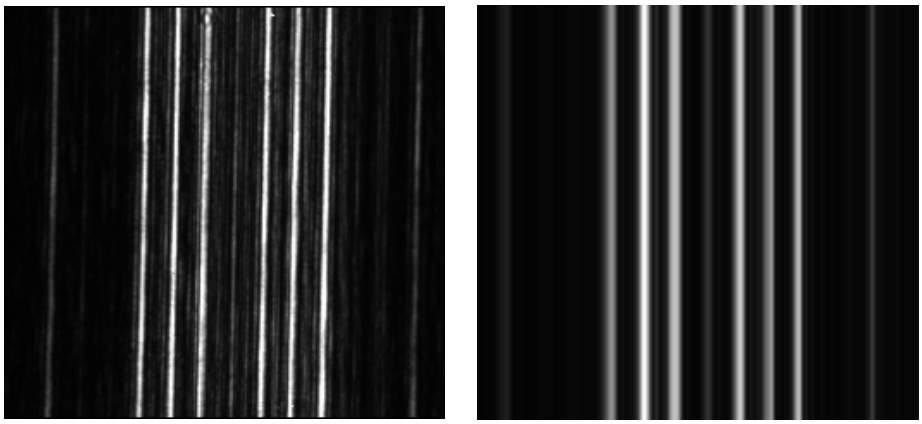

(a) **(b)**

Figure 3.7: Far-field image of Dammann grating captured with a conventional lens **(a)** and imaging thread **(b)**

in the back focal plane of a lens behind the projection system, is shown in Fig. 3.7 a. The image captured by the imaging thread is shown in Fig. 3.7 b. Although the scan was one-dimensional, the data is artificially expanded to two-dimensions for easy comparison to **(a)**. The relative intensities and locations of the peaks are in reasonable agreement. The peaks are slightly wider for the imaging thread because it had lower far-field resolution than the lens.

3.4 Coupling Efficiency

There are three illumination conditions under which the imaging threads may be used. These include coherent objects, incoherent objects, and an active LIDAR-like mode. Each of these have very different optical throughputs.

Under coherent illumination, like the experiments above, the coupling efficiency is given by the overlap integral

$$\eta = \frac{\left|\int A^*(x,y)B(x,y)dS\right|^2}{\int |A(x,y)|^2\, dS \cdot \int |B(x,y)|^2\, dS}, \tag{3.16}$$

where $*$ indicates the complex conjugate, dS is the infinitesimal area element, A is the amplitude point spread function, and B is the field in the object plane. The overlap integral is the same as the imaging skin, but the point spread functions of the two systems are quite different. Specifically, the PSF for the imaging thread has a large extent in one dimension. The phase, given by Eq. 3.7, changes along that dimension. Therefore, an object with uniform phase will have very low coupling efficiency. If the mode exits normal to the fiber, $\theta_c = \pi/2$, a cylindrical lens can be used to match the phase.

Consider an object consisting of a continuum of mutually incoherent point sources. The power in the waveguide mode at each scan location is given by the convolution of the object intensity with the intensity point spread function (IPSF). The shape of the IPSF is shown in Fig. 3.5, but the maximum coupling efficiency has yet to be determined. It is shown in section 2.2, as long as the object distance is greater than the Rayleigh range, the efficiency is dominated by the solid angle of the aperture. Specifically, the measured power is

$$P \leq \frac{P_i A}{4\pi d_o^2} dxdy, \tag{3.17}$$

where A is the projected aperture area, P_i is the total power emitted by the point, and d_o is the object distance. For example, a $1\,cm$ imaging thread on SMF-28 fiber, at best, can receive 0.0820% the power received by a similarly sized imaging skin. As the aperture width goes to zero, so does optical throughput.

A third option is to actively illuminate the object. A laser end-fired into the fiber couples out of the grating and illuminates the object only within the system's point spread function. The specular reflections from the object will have the complex conjugate phase of the input PSF and therefore have very low coupling efficiency. The diffuse reflections are mutually incoherent and will add in intensity. An active illumination system can boost optical throughput by increasing the illumination efficiency.

3.5 Conclusions

It has been shown that a high resolution imaging system can be confined to a nearly one-dimensional form factor. Specifically, scanning a tilted fiber Bragg grating on a single-mode optical fiber was able to resolve narrow grating diffraction orders. The decrease in aperture width came at the expense resolution in one of the spatial dimensions. In general, the PSF lies on an ellipse in the object plane. If the grating tilt angle is 45°, the Bragg condition requires normal incidence and the PSF is a line segment. Reducing the pupil area also significantly decreases the optical throughput. The coupling efficiency under incoherent illumination is linearly proportional to the width. To overcome the decrease in optical throughput, an active system which increases illumination efficiency has been proposed.

Chapter 4

Polychromatic Imaging

Up to this point, monochromatic light has been assumed. The systems, as described, are shown to have large chromatic dispersion which greatly reduces resolution under polychromatic illumination. Any system can be made pseudo-monochromatic by adding a narrow spectral filter just before detection. The narrower the filter, the lower the optical throughput. Therefore, the design of an efficient filter requires quantitative knowledge of the chromatic dispersion. Even with filtering, imaging skins and threads have a limited band of usable wavelengths. The many spectral constraints are explored. Finally, different modes of operation are suggested which vary in their utilization of the polychomatic information.

4.1 Dispersion

Imaging skins and threads both employ grating couplers on waveguides. As a result, they share the same three types of chromatic dispersion. Material dispersion, the change in refractive index of the bulk material, is generally small for low loss dielectrics. The modal dispersion, the change in modal effective index, is typically larger than the material

dispersion. The largest dispersion comes from the grating coupler. All three types of dispersion are explored independently and together.

Material dispersion is commonly described by the Sellmeier equation,

$$n^2(\lambda) = 1 + \frac{B_1\lambda^2}{\lambda^2 - C_1^2} + \frac{B_2\lambda^2}{\lambda^2 - C_2^2} + \frac{B_3\lambda^2}{\lambda^2 - C_3^2}, \tag{4.1}$$

where B_1, B_2, B_3, C_1, C_2, and C_3 are empirically determined constants for a particular material. The coefficients for common materials are given in table 4.1. The refractive index and its derivative with respect to wavelength, for each material, are shown in Fig. 4.1. As the wavelength decreases, the magnitude of the dispersion increases. Over the entire visible spectrum, the dispersion remains quite small.

Material		B_1	C_1	B_2	C_2	B_3	C_3
Silicon Nitride	[36]	2.894	0.1397				
Fused Silica	[37]	0.6962	0.06840	0.4079	0.1162	0.8975	9.896
Aluminum Oxide	[38]	1.4313	0.07266	0.6505	0.1193	5.341	18.03
Hafnium Oxide	[39]	1.956	0.1549	1.345	0.0634	10.41	27.12

Table 4.1: Sellmeier coefficients of common waveguide materials

The mode effective index changes with wavelength even when there is no material dispersion. Mode dispersion does not have a known analytic description, however the relation can be determined numerically by solving the eigenvalue equation at different wavelengths. The effective index, shown in Fig. 4.2 (a), is calculated for the TE0 mode of the planar guide used in the imaging skin. To show the effect of material dispersion, the mode effective index was calculated using the material indices from the Sellmeier equations and the average of these indices over the wavelength band. As expected, n_{eff} is between the core and cladding index. For short wavelengths, n_{eff} is close to the index of the core. As the wavelength becomes larger, mode confinement decreases and the effective index approaches the index of the cladding. Therefore, low index contrast guides generally have smaller mode dispersion compared to a high

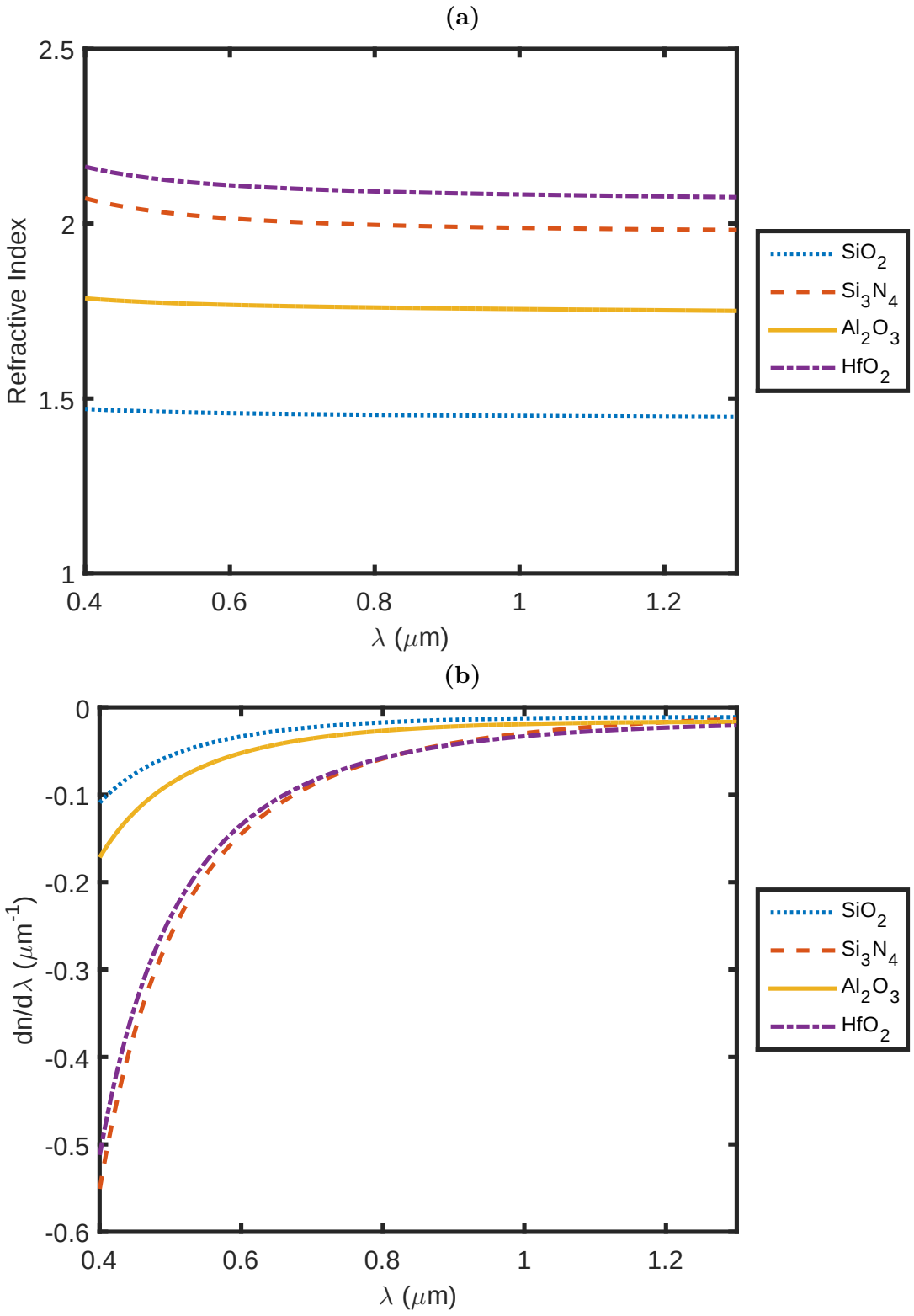

Figure 4.1: Refractive index **(a)** and the derivative of refractive index with respect to wavelength **(b)**

contrast guide. The mode dispersion, given by the derivative of the effective index with respect to wavelength, is shown in Fig. 4.2 (b). For this particular waveguide, material dispersion can be ignored when working in the near IR. In the visible band, the nitride's material dispersion becomes significant.

The grating coupler is an additional source of chromatic dispersion. Recall that the angle of the out-coupling mode, with respect to the surface normal, is

$$n_0 \sin\theta = n_{eff} - q\frac{\lambda}{d}, \tag{4.2}$$

where n_{eff} is the effective index of the mode, q, d, and λ are the diffraction order, grating period, and wavelength respectively. The angle dispersion is the derivative of Eq. 4.2 with respect to wavelength, which after some simplification is

$$\frac{d\theta}{d\lambda} = \frac{1}{n_0 \left|\cos\theta\right|}\left(\frac{dn_{eff}}{d\lambda} - \frac{q}{d}\right). \tag{4.3}$$

The dispersion is linearly proportional to the diffraction order and is minimized when the mode exits normal to the guide. As shown in Fig. 4.2 **b**, the mode dispersion for the nitride waveguide is negative for all wavelengths of interest. Because the two terms have the same sign, it is not possible to compensate the grating dispersion with modal dispersion.

As another example, the dispersion was measured for a TFBG on a SMF-28 fiber. A tunable laser was end-fired into the fiber while the far-field radiation pattern was measured in the back focal plane of a $19\,cm$ lens. The angle was calculated by dividing the shift in the pattern by the lens focal length as shown in Fig 4.3. The measured angle was compared to Eq. 4.2 using $n_{eff} = 1.467$, $d = 1.392\,\mu m$, and $q = 2$. The difference in slope is the result of the small error in effective index. Even using the zero-order model for n_{eff}, the dispersion curve is a good match to the measurement.

It is possible to compensate material and mode dispersion over a narrow spectral band. Dispersion compensated fibers have been implemented by germanium doping the

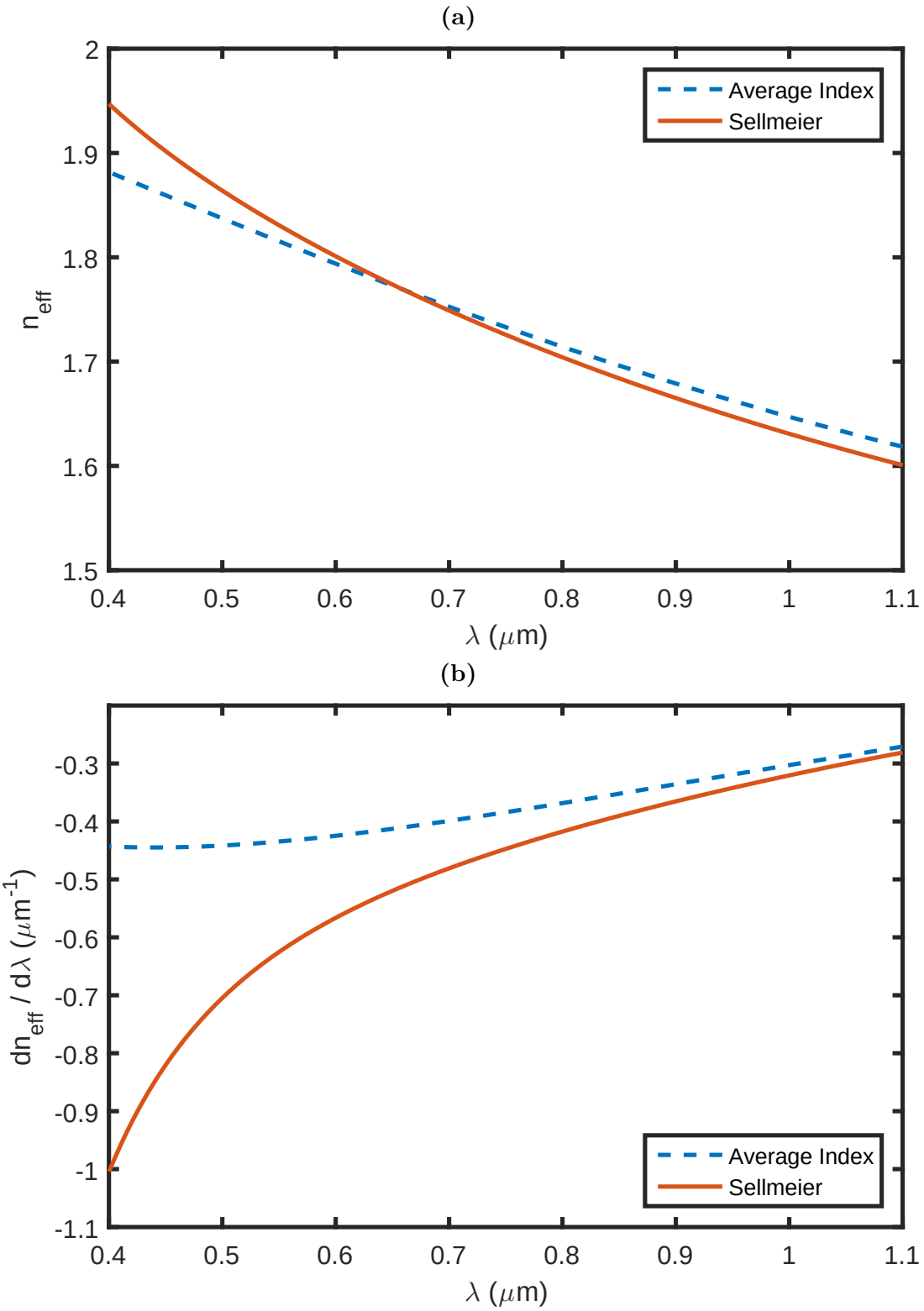

Figure 4.2: **(a)** Effective index and **(b)** mode dispersion vs wavelength

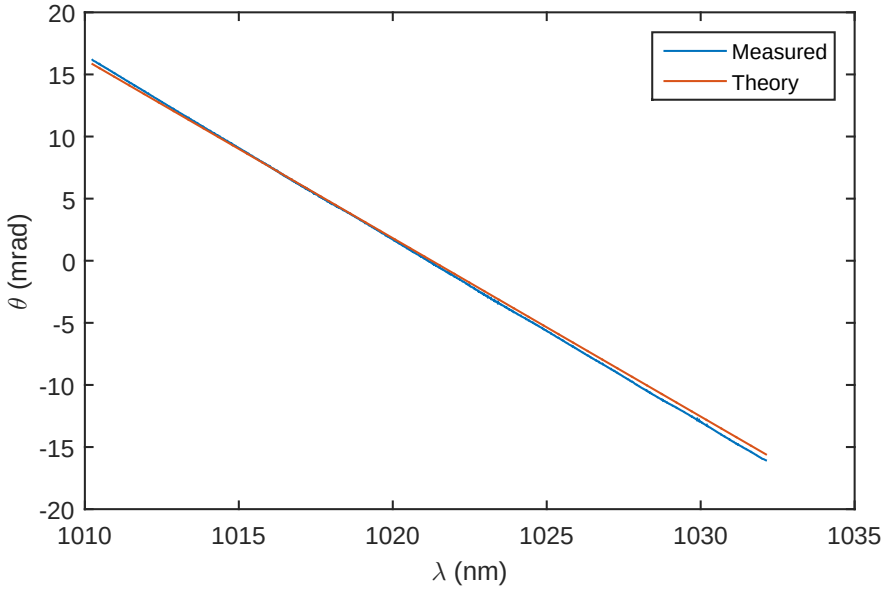

Figure 4.3: Chromatic dispersion of TFBG of fiber

core [40], using double and triple claddings [41], and photonic crystal guides [42]. These techniques, however, are not capable of compensating the large dispersion introduced by the grating. A method for achromatizing the diffraction angle has been proposed which uses a second grating [43]. This method, however, can not be made planar. Until an achromatic waveguide coupler is developed, the spectrum must be narrowed to maintain far-field resolution.

4.2 Spectral Resolution

The spectral resolution of the system corresponds to the change in wavelength ($\Delta\lambda$) which shifts the pattern by one Rayleigh resolvable spot. Assuming $L_c > L_g$, the angle width is

$$\Delta\theta = \frac{\lambda \cos\theta}{Lg}. \tag{4.4}$$

For small change in wavelength $\Delta\lambda$, the change in angle is

$$\Delta\theta \approx \frac{d\theta}{d\lambda}\Delta\lambda. \tag{4.5}$$

Equating Eqs. 4.5 and 4.4, substituting Eq. 4.3 for $d\theta/d\lambda$, and performing some algebraic manipulation, the spectral resolution is

$$\left|\frac{\Delta\lambda}{\lambda}\right| = \left(q - d\frac{dn_{eff}}{d\lambda}\right) N, \tag{4.6}$$

where $N = L_g/d$ is the number of grating lines. If the waveguide has no modal dispersion, Eq. 4.6 becomes the known spectral resolution for a standard diffraction grating [2],

$$\left|\frac{\lambda}{\Delta\lambda}\right| = qN. \tag{4.7}$$

To get a sense of scale, the spectral width is calculated for the imaging skin presented in Ch. 2. From Fig. 4.2, n_{eff} and $dn_{eff}/d\lambda$ are 1.783 and $-0.5347\,\mu m^{-1}$ respectively when $\lambda = 632.8nm$. The grating period d is $460\,nm$, the grating length L_g is $1\,cm$, and first order diffraction, $q = 1$, is assumed. Evaluating Eq. 4.6 gives

$$\Delta\lambda = 23.36\,pm. \tag{4.8}$$

If the object intensity is uniform over the visible range, the spectral filter needed to maintain far-field resolution would have a $41.1dB$ loss in available power.

In a lens based imaging system, increasing the lens diameter simultaneously increases the angular resolution and the optical throughput. To achieve resolution gains in a grating-coupler based imaging system, an increase in aperture width must be accompanied by a proportional decrease in spectral bandwidth. Assuming the object spectrum is uniform, the power gains from increasing the aperture are lost by the bandwidth reduction. For an imaging skin with a Rayleigh limited spectral filter, increasing L_g can increase throughput by leaving the spectral bandwidth fixed. Such an aperture

enlargement, however, would offer no resolution improvement. A designer can trade off optical power for resolution and vice versa, but for a fixed size aperture, can not simultaneously increase both.

4.3 Chromatic Range

In any imaging system, the range of usable wavelengths is limited by the responsivity of the detector and material absorption. Imaging skins and threads have additional, often more restrictive, limits. Many of the same design constraints discussed previously for a single wavelength also limit the spectral width. Here, the relevant inequalities are solved for λ. Many of these constraints are similar for fibers and slab waveguides, so they will be treated together. The differences between the two systems are more often the result of grating type, thin vs Bragg, and have little to do with the camera's form-factor.

The primary requirement of any waveguide is that it supports a guided mode. In symmetric structures, where the superstrate and substrate have the same index of refraction, there is no lower cutoff for V number [16]. To ensure the TE0 mode is supported in an asymmetric guide,

$$\lambda < t_{core} \frac{2\pi\sqrt{n_1^2 - n_2^2}}{\arctan\left[\sqrt{n_2^2 - n_0^2}/\sqrt{n_1^2 - n_2^2}\right]}. \tag{4.9}$$

As the wavelength decreases, the V number and the number of supported modes increases. Multiple modes would result in ambiguity in angle. The TE1 and all higher TE modes are cutoff if

$$\lambda > \frac{2\pi t_{core}\sqrt{n_1^2 - n_2^2}}{\arctan\left[\sqrt{n_2^2 - n_0^2}/\sqrt{n_1^2 - n_2^2}\right] + \pi}. \tag{4.10}$$

For the same reason, the TM_0 and the other transverse magnetic modes should be cutoff. The preference for TE_0 over TM_0 is because if the former is cutoff, the later is

also. The TM_0 cutoff condition is

$$\lambda > \frac{2\pi t_{core}\sqrt{n_1^2 - n_2^2}}{\arctan\left[\frac{(n_1^2/n_0^2)\sqrt{n_2^2-n_0^2}}{\sqrt{n_1^2-n_2^2}}\right]}. \tag{4.11}$$

Because fibers are symmetric, at least one guided mode will be supported for any wavelength. To keep the wave well confined, the wavelength should be smaller than the core diameter. A single-mode condition, similar to the planar waveguide, also exists. For all fibers, the multi-mode V-number cuttoff is 2.405 [32] which means

$$\lambda > \frac{2\pi a\sqrt{n_1^2 - n_2^2}}{2.405}, \tag{4.12}$$

where a is the core radius. These conditions are not overly restrictive. For example, a fiber with the same index profile as SMF-28 but a core less than $3.57\,\mu m$ would support one and only one mode over the entire visual spectrum.

The single diffraction order requirement is typically much more limiting compared to the single mode requirement. To have one, and only one, diffraction order in the air

$$d/2\,(1 + n_{eff}) \leq \lambda \leq d\,(1 + n_{eff})\,. \tag{4.13}$$

Requiring a single diffraction order in the substrate increases coupling efficiency, but is not essential. Disallowing a second substrate order requires

$$\lambda \geq \frac{d}{2}\,(n_2 + n_{eff})\,. \tag{4.14}$$

Because n_{eff} is wavelength dependent, it is often convenient to use the more restrictive conditions found by replacing the effective index with the core or cladding index. Specifically, Eqs. 4.13 and 4.14 can be replaced by

$$d/2\,(1 + n_1) \leq \lambda \leq d\,(1 + n_2) \tag{4.15}$$

$$\lambda \geq \frac{d}{2}\,(n_2 + n_1)\,. \tag{4.16}$$

Substituting the indices and period from the imaging skin, the effective range is $679.8\,nm \leq \lambda 1.140\,\mu m$. To move to the visible band, the grating period would need to be decreased.

Bragg gratings, such as the TFBG, can be designed to work at higher diffraction orders. The TFBG used in the imaging thread experiment, for example, had its second diffraction order near the Bragg peak. Because the first order was not well Bragg matched, very little power coupled in through this order. The higher diffraction orders tend to have low coupling efficiency. Therefore, it is preferable to use the first order.

For the TFBG, the most restrictive limits on wavelength range tend to come from the Bragg match condition. According to [35], the wavelength dependence on coupling efficiency is described by the longitudinal phase mismatch. A closed form solution for the spectral width of a radiating mode out-coupled from a TFBG has not yet been determined. The spectrum can be calculated numerically by either the volume current method [35] or coupled mode analysis [44] . It is known that the spectrum depends on the core diameter, but not the grating length [45]. Specifically, the larger the core, the smaller the bandwidth. By end-firing a tunable laser into the imaging thread, it was shown experimentally that the spectrum was wider than $30\,nm$.

In both the imaging skins and threads, the wavelength bandwidth is significantly narrower than the responsivity of a silicon detector. An imaging device using a thin grating, with careful choice of the waveguide parameters and grating period, can span the visible spectrum. An external filter must be used to prevent a wavelength with multiple diffraction orders from contaminating the signal from those with single diffraction order. In contrast, the Bragg gratings have a much narrower bandwidth. Because this bandwidth is set by a reduction in coupling efficiency, there is no need for an additional bandpass filter.

4.4 Polychromatic Systems

There are several approaches to polychromatic imaging. The panchromatic image, where the detected power at each point is a weighted sum of all wavelengths, is not practical for grating based imaging systems because of the large chromatic dispersion. The system can be made pseudo-monochromatic by adding a narrow spectral filter. One could also replace the single filter and detector with a spectrometer. If the object spectrum is known apriori, the angle information is encoded in wavelength and there is no need to mechanically scan the system. By mechanically scanning, the grating-spectrometer hybrid system builds a hyperspectral image. From the hyperspectral information, an achromatic or standard RGB image can be created for human consumption.

The power could be coupled to a bulk spectrometer, but this would violate the spirit of the work: to confine the system to a plane or line. Waveguide grating couplers have been used as spectrometers [46]. To have sufficient spectral resolution, the number of lines on the spectrometer grating must be greater than or equal to the number of lines on the imaging grating. These systems also require the detector be placed out of the waveguide plane. Several planar spectrometers have been developed including arrayed waveguide gratings [47] and a static Fourier transform spectrometer [48]. Fiber Bragg gratings can be used as spectrometers and have a linear form factor [45].

Instead of spectrally filtering the waveguide modes, the effects of chromatic dispersion can be mitigated by illuminating the object with monochromatic light. For example, light from a tunable laser can be coupled to the waveguide mode and out the imaging grating. The out-coupling intensity profile would match the intensity point spread function of the system at that wavelength. Because the illumination is confined to the current object point, the illumination efficiency is maximized. So long as the illumination is much brighter than background light, the system is essentially monochromatic. If the object reflectivity is uniform in wavelength, this system also

does not require mechanical scanning. Tunable lasers can be monolithically integrated on the planar waveguide [49], maintaining the small system form-factor.

4.5 Conclusions

The grating coupler imaging systems have significant chromatic dispersion. Though techniques have been developed which reduce it, no technique is known to eliminate dispersion while maintaining the planar form factor. This dispersion requires that spectral filtering occur before detection. The higher the far-field resolution, the narrower the required spectral width. Planar spectrometers already exist which can be used to capture all wavelengths simultaneously. If the object spectrum is known apriori, the wavelength encodes angle and eliminates the need for mechanical scanning. With a spectrometer and mechanical scanning, the imaging threads and skins become hyperspectral imaging systems with high spectral and far-field resolution.

Chapter 5

Waveguide Multiplexing

Scanned systems, like the imaging skins and threads, divide the frame period among the N points of the object. For a given brightness, reducing the integration time at each point tends to decrease the signal to noise ratio (SNR). Specifically, a shot-noise limited detector has an SNR which is proportional to the square root of the number of received photons. Given the same scene and SNR requirement, a scanned system will have a frame period N times longer than a lens which captures all points in parallel. Spatial mode multiplexing is explored as a means of parallelizing image capture to increase frame rates or SNR.

In confocal microscopy, it is common to use multiple apertures to capture many points simultaneously as illustrated in Fig. 5.1. For M pinholes, the scan time is decreased by a factor of M while maintaining the spatial resolution and SNR. A spinning Nipkow disc is a convenient choice of aperture because it allows for simple mechanical scanning [50]. Without this parallelism, volumetric scans would be impractical.

A waveguide, should its V-number be high enough, can support multiple spatial modes. Ideally, these modes are independent and can act as separate communication channels. The unique effective index of each mode corresponds to a distinct angle in

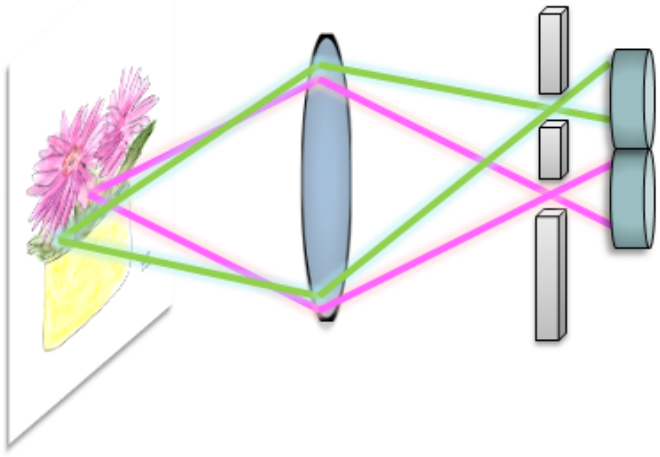

Figure 5.1: Multiple aperture confocal imaging

the far-field. If they are isolated before detection, multiple spatial modes are analogous to the multiple apertures used on confocal systems.

5.1 Grating Couplers on Multimode Planar Waveguides

A planar waveguide can support multiple modes if the core is sufficiently thick. For example, a Nitride on Silicate waveguide with a core thickness of $600\,nm$ supports five modes at $\lambda = 632.8\,nm$. The effective index for each mode can be found by solving the characteristic equations given in Ch. 2. The grating period can then be chosen using the inequality graph shown in Fig. 5.2. The effective indices are shown as horizontal lines. So that each mode couples to a single diffraction order in air, $1.65 \leq \frac{\lambda}{d} \leq 2.47$, or

$$256.3\,nm \leq d \leq 383.5\,nm. \tag{5.1}$$

As the number of supported modes increases, the range of allowed grating periods decreases.

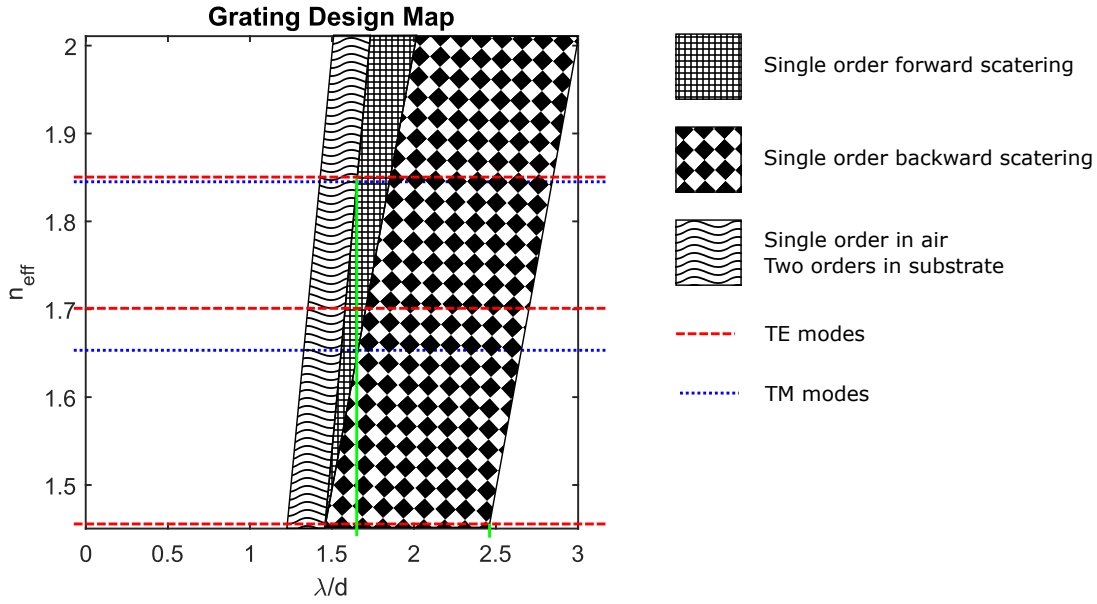

Figure 5.2: Grating design window for a multimode guide

For a uniform period, linear grating each mode corresponds to a unique angle. The range of possible angles is determined by the material system and grating period. Because it generally has a larger range of effective indices, a high index contrast guide has a narrower angle spread compared to a low contrast guide with the same grating period. Adding additional modes, by increasing the width of the core, would decrease the spacing between the modes but have little effect on angle range. The angles for each mode of the example planar waveguide, when the grating period is $316.4\,nm$, is summarized in the table 5.1. If the grating is $1\,cm$ long, the smallest difference in angle between modes is about 190 resolvable spots apart. The largest difference is over 3120 resolvable spots. As in this example, the angle spacing between the modes is almost never uniform.

Mode	n_{eff}	θ_0 (degrees)
TE0	1.8522	-8.4995
TE1	1.7060	-17.0976
TE2	1.4698	-32.0190
TM0	1.8403	-9.1895
TM1	1.6610	-19.8160

Table 5.1: Coupling angles for a multimode guide

5.2 TFBG on Multimode Optical Fiber

Optical fibers can also have multiple spatial modes. To demonstrate the angle dependence of each mode, an argon laser was coupled into the same TFBG described earlier. At $\lambda = 514.5\,nm$, this fiber is known to have six modes. The angle was again scanned by translating the collimating lens. The field exiting the fiber end-facet was captured on a CCD. The normalized intensity in Fig. 5.3 corresponds to the sum of the pixel in each frame. The included frames at the local maxima match the known intensity distributions of the LP Modes.

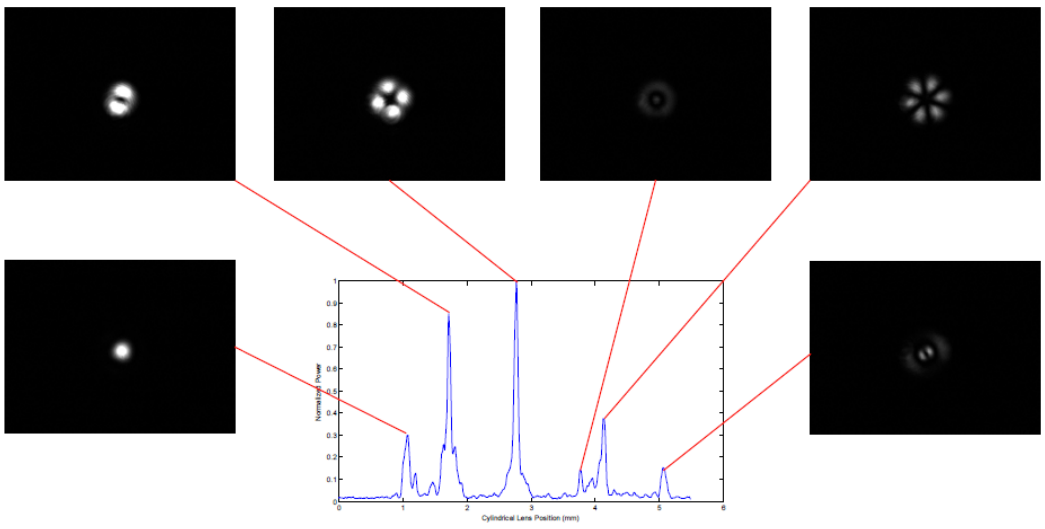

Figure 5.3: Mode exiting end-facet while coupling into TFBG at different angles

As shown in Fig. 5.3, each mode has a different angular width and coupling efficiency. The difference in the resolution has two main sources. First, the resolution is inversely proportional to $\cos\theta_0$. This is a small effect for the low index contrast optical fiber, but can be quite large for a high index guide. The modes also have different coupling lengths. L_c is related to the degree of Bragg mismatch and the mode's spatial profile. The difference in coupling length is also the largest contributor to the variation in coupling efficiency. These effects can be numerically compensated when merging the different modes into a single image.

5.3 Mode Separation

To parallelize image capture, the spatial modes must be separated before detection. Several techniques exist for isolating waveguide modes. An optical matched filter method is described in [51] and is expanded on by [52]. Though effective, this technique can not be implemented in a low-dimensional form-factor. A second approach is to use a second grating coupler as a modal filter. As shown in Fig. 5.3, the grating maps each spatial waveguide modes into a discrete angle. A small lens can then map these angles to points on a detector array. This method also cannot be made perfectly flat because the out-coupled field must come to a focus in some other plane. The image side resolution need only be high enough to separate the modes, which can be achieved with thin micro-optics. This is analogous to the confocal system where the detector area is just small enough to see power from a single aperture.

An example mode extractor is designed for the planar guide described earlier. The design of the mode separation grating is similar to the design of the object side grating. The grating length needed to just resolve the separate modes is

$$D \geq \frac{\lambda}{\tan\Delta\theta_{min}}, \tag{5.2}$$

where $\Delta\theta_{min}$ is the minimum separation in angle of the modes. For our example $\Delta\theta_{min} = 0.69^\circ$ and $D \geq 52.54\mu m$. To maintain the efficiency, the coupling length should be

$$L_c = \frac{L_g}{1.25643}. \tag{5.3}$$

It is possible that the desired coupling length is too short to be practical for the waveguide system necessitating a larger grating length. The lens diameter must also be greater than or equal to the grating length. The focal length of the lens must be

$$f \geq \frac{\Delta x}{\tan \Delta\theta}, \tag{5.4}$$

where Δx is the pixel separation. If the array has a $10\,\mu m$ pitch, for example, the minimum focal length is about $1\,mm$. This $f/19$ lens can be made with a singlet microlens with low aberrations. The resulting system will be significantly larger than the wavelength, but is smaller than other systems with similar angle resolution.

5.4 Mode Cross Talk

Imperfections in the waveguide result in mode mixing; power from one mode couples into another. Parallel image capture using multiple spatial modes requires the channels to be independent. Specifically, the mode mixing is assumed to be negligible. To verify this assumption, the mode mixing was measured using the setup in Fig. 5.4. Two TFBGs separated by one meter were written on a single piece of SMF-28 fiber. A collimated argon laser was focused down to the input grating by cylindrical lens L_3. A second cylindrical lens, L_4, pseudo collimated the out-coupled light from the output grating before passing through a spherical lens, L_2. A CCD was placed in the back focal plane to capture the power per output angle. The collimating lens, L_1, was scanned to change the input angle.

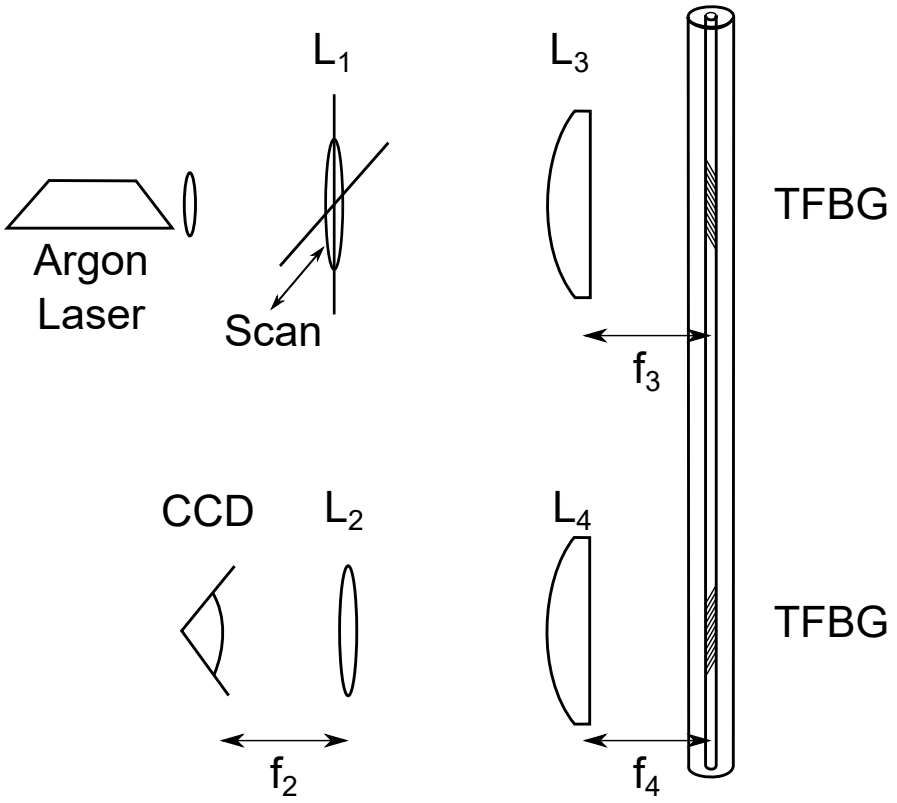

Figure 5.4: Setup for measuring mode cross talk

The measured power for each input and output angle is shown in Fig. 5.5. The image is inverted, so the darker pixels correspond to higher power. There are four input angles which have significant output power. The maxima in power occur along a diagonal in regions separated by the same output angle spacing as the input. These regions represent the power which remained in its respective mode. The regions off the main diagonal represent cross-talk.

The same data shown in Fig. 5.5 can be analyzed to give a quantitative measurement of mode mixing. The data is divided into a grid where the power at each location is given by the sum of the pixel values in that region. The power was then normalized by the sum of the power in all regions. Because we are interested in the percent power

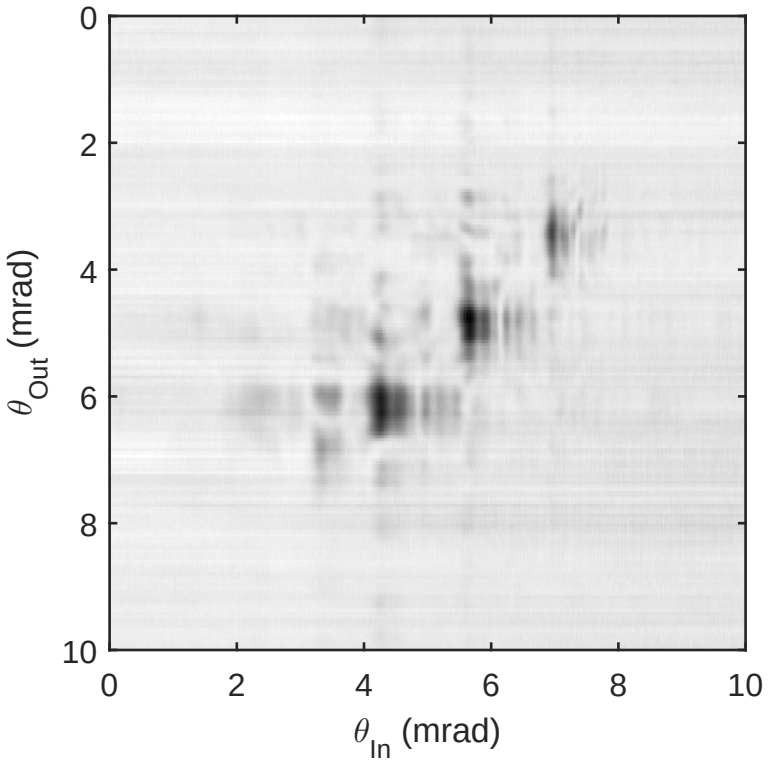

Figure 5.5: Map of power for each input/output angle

that transferred to each mode, the power was normalized by the sum of all regions corresponding to a given input angle. The measured mode mixing is summarized in table 5.1. Even for a $1\,m$ length of fiber, the cross talk is significant. The percentage of power which remains in a single mode was always less than 66%. The coupling from one mode to another was as high as 31%. Mode cross talk leads to ambiguity from which angle the power came. Assuming the cross talk matrix is constant throughout the scan, it is possible to undo the effect numerically. Such an inversion would require high SNR.

InMode/OutMode	1	2	3	4
1	0.4541	0.3123	0.1784	0.0552
2	0.3118	0.4959	0.1373	0.0550
3	0.1541	0.0829	0.5946	0.1684
4	0.1738	0.0634	0.1078	0.6550

5.5 Polarization Dependence

The coupling efficiency for a 45° grating has been shown to be as much as $40dB$ higher for the S vs the P polarization states [35]. For the single mode thread, this meant that only one of the polarization states could be effectively coupled. For the two grating design, the polarization direction of the mode must be maintained between the object and image gratings. A polarization maintaining fiber could be used for this purpose, but extra care must be taken that the gratings align to the polarization direction. The polarization mechanism, typically stress induced birefringence, must also not occlude the core during the grating fabrication. As of the time of writing, the author is not familiar with any instance where such a grating has been made. Therefore, the limits of standard fiber are explored.

The fiber must be sufficiently short such that the polarization direction does not rotate between the object and image gratings. Such a length depends on random internal stresses in the fiber or external bends, and is therefore hard to predict. The polarization rotation, however can be measured experimentally using a TFBG. The setup for this procedure is shown in Fig. 5.6. The linear polarization of the Argon laser is rotated by the half wave plate before end-firing into the fiber with a 40x object, L_1. After propagating through the fiber and out-coupling through the grating, the field is pseudo-collimated by the cylindrical lens, L_2. The discrete angles are converted to points on the CCD by lens L_3.

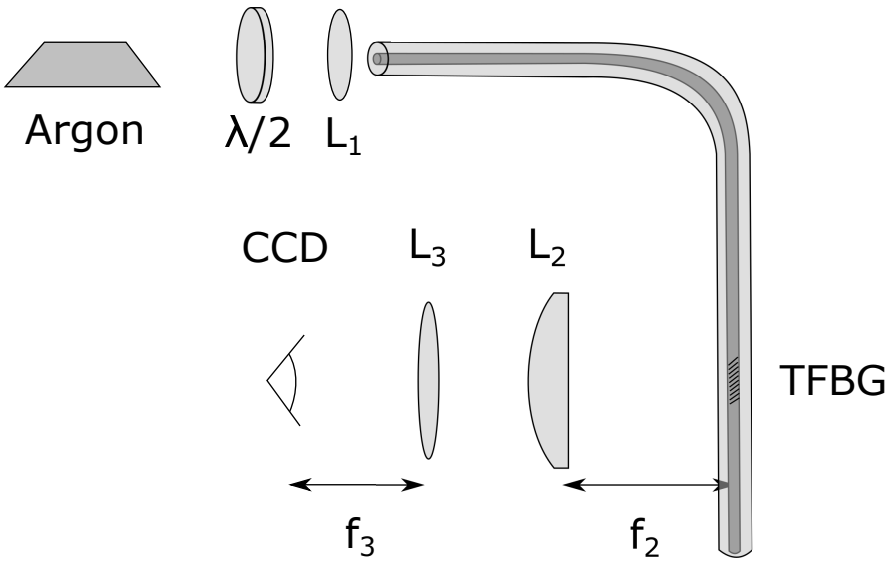

Figure 5.6: Experimental setup for measuring polarization rotation

The half wave plate rotates the incoming linear polarized light as

$$\psi = 2\phi, \tag{5.5}$$

where ϕ is the angle between the input polarization angle and the fast axis. Setting the reference angle to be the fast axis, ϕ is also the rotation angle of the plate. Because the P polarization state is so weakly coupled, the output grating acts as a linear polarizer which obeys Maulus' law

$$I = I_0 \cos^2 \psi. \tag{5.6}$$

Power at each output angle θ was measured as the half wave plate was rotated in 10° increments as shown in Fig. 5.7. Four distinct modes are visible. The power of each mode is a periodic function of the wave plate rotation angle ϕ with a frequency of 4, but different phase.

The absolute rotation is less important than the relative polarization angle. The relative phase of each mode, summarized in table 5.2, is measured by performing a fast

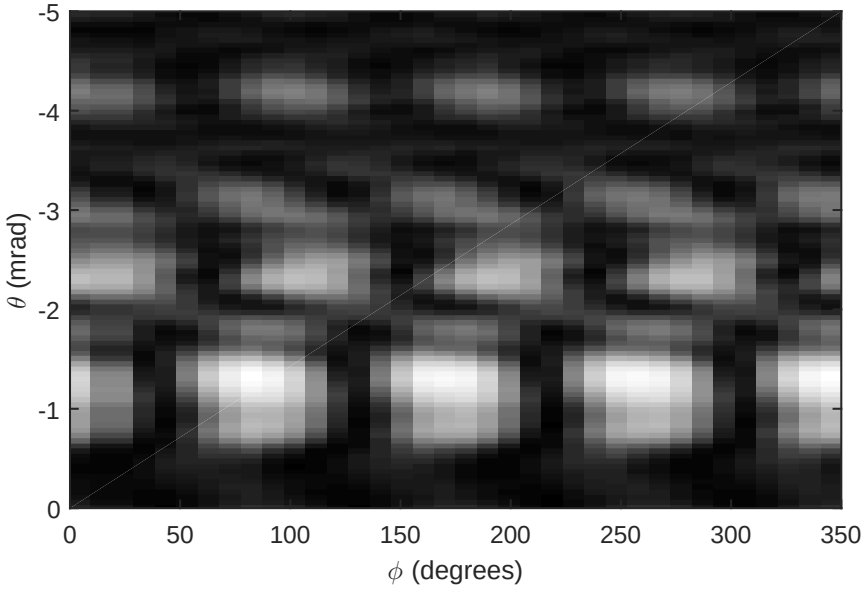

Figure 5.7: Measured power along output angle θ for a given rotation angle ϕ of the half-wave plate

Fourier transform. The largest difference in phase is 1.44, or just under $\pi/2$ which corresponds to the orthogonal polarization. If a second grating was added and aligned so mode two efficiently coupled, the coupling of the first mode would be very small. For a non-polarization maintaining fiber, the polarization rotation can not be eliminated. However, reducing the distance between the gratings generally reduces the polarization rotation. The rotation of polarization angles between the two gratings limits the coupling efficiency for Bragg gratings.

Mode	Phase (rad)
1	-0.5043
2	0.9356
3	0.8864
4	0.6758

Table 5.2: Relative phase of polarization angle for each mode

5.6 Dual Prism Coupler Experiment

Parallel imaging using mode multiplexing was experimentally verified using two prism couplers on a slab waveguide. Like grating couplers, prisms with an index of refraction greater than the waveguide core can couple points in the far-field into waveguide modes. Although the prisms make the system non-planar, the mounts needed to keep the prism a fixed distance from the waveguide surface provide a convenient method of blocking scattered light. The experimental setup is shown in Fig. 5.8. The waveguide in this experiment was a solgel material which has a low index contrast. The beam from a HeNe laser is collimated by lens L_1 before passing through a pseudo-random barcode cut out of cardboard. Lens L_2 Fourier transforms the barcode pattern in the plane where the first prism meets the waveguide. Lens L_3 maps the distinct angles out-coupling from the second prism to points on the CCD. Scanning was performed by mechanically translating the barcode.

The angles were aligned to the x-direction of the CCD, so the pixels could be summed along the y-direction to yield the two dimensional image in Fig. 5.9. The four waveguide modes appear as bands in the vertical direction. In the horizontal direction, the barcode pattern repeats in each of the modes. There is a discontinuity at $x = 24.8\,mm$ where the barcode accidentally shifted. The lens was aligned to the lowest order mode and comes into sharp focus. The higher modes, however have increasing degree of aberration. Note the bottom most mode has so much comma that it has some overlap with the mode above it.

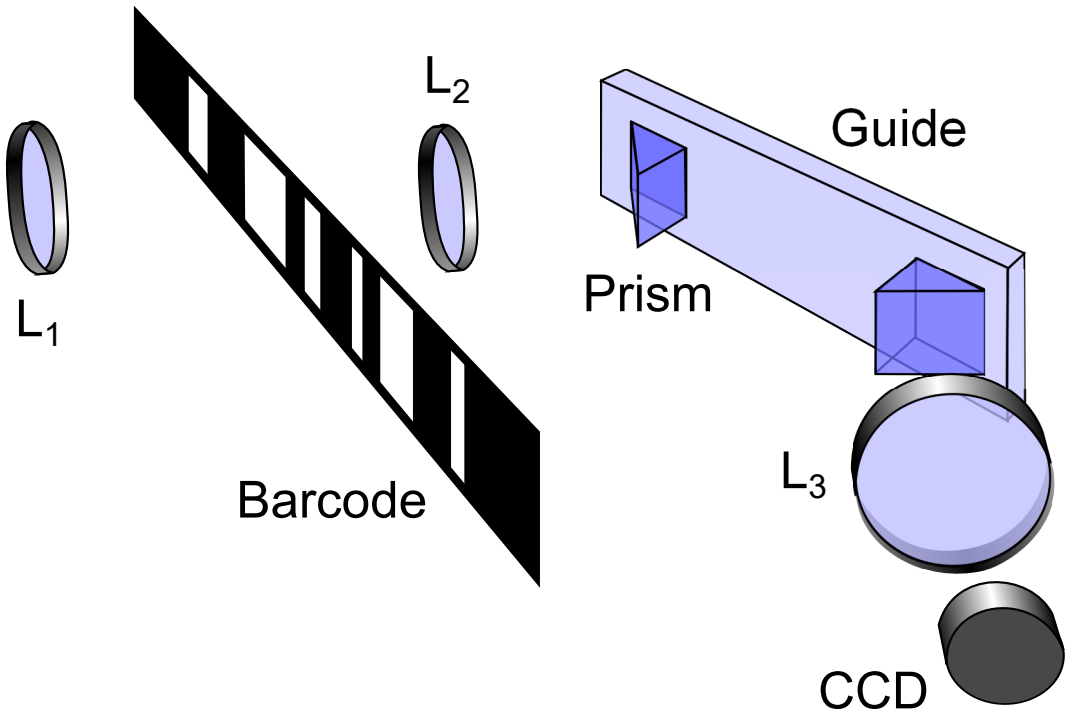

Figure 5.8: Dual prism coupler multimode imaging experiment

5.7 Conclusions

Multi-point image capture was demonstrated using the multiple modes of a waveguide. This technique is similar to a muli-aperture confocal system where each mode corresponds to a separate aperture. Specifically, each mode has a unique effective index and therefore corresponds to a distinct angle. The difference in angle between the different modes tends to be wider for high index contrast of the guides. Assuming the modes can be isolated before detection, the frame rate can be drastically improved for a given signal to noise ratio. One method of separating the modes is to use a second grating and a lens. The resolution on the image side need only be high enough to resolve the modes. The system is not strictly planar, however low-profile micro-optics can be used.

There are several design considerations in making a dual grating imaging system.

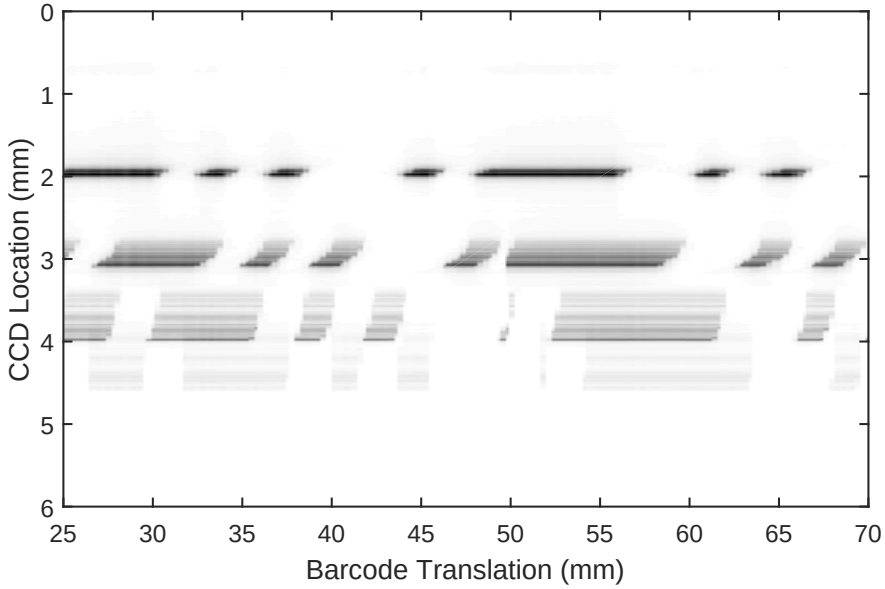

Figure 5.9: Power vs angle as a pseudo-random barcode is translated in front of dual prism coupler setup

The longer the distance between the gratings the higher the degree of mode cross-talk. The larger the number of modes the higher the optical throughput, but the lower the range of usable grating periods. It is possible that no grating period will have a single diffraction order in the air for all modes. Bragg gratings, such as the TFBG, are very sensitive to polarization. To maintain high efficiency, the polarization angle of the LP modes must not rotate between the two gratings.

Separating the modes in the polychromatic case is particularly challenging. The chromatic dispersion causes different modes at different wavelengths to correspond to the same angle. Not only do the effective indices change, the number of modes is a function of wavelength. For monochromatic or active illumination, multiple waveguide modes is a good option for increasing the frame rate of the imaging skins and threads.

Chapter 6

Finite Conjugate Imaging System

Up to this point, the imaging skins and threads have been designed to work at infinite conjugates; the object is at infinity. Grating couplers can have any conjugate ratio. In addition to being able to image an object closer than the Rayleigh range, a finite conjugate system can have a spot size smaller than the aperture.

Focusing grating couplers, FGCs, come in several varieties. A chirped grating, where the grating period is a function of position, will focus a waveguide mode into a line [53]. By curving the grating lines, in addition to changing period, one can map a planar waveguide mode to a converging spherical wave [54]. While the two-dimensional focusing grating has been explored as an optical pickup [55], FGCs have yet to be employed for general purpose imaging. Because the limitations of FGCs are similar whether focusing occurs in one or two dimensions, this discussion will be limited to the straight-line chirped gratings which are easier to design and analyze than the curved gratings.

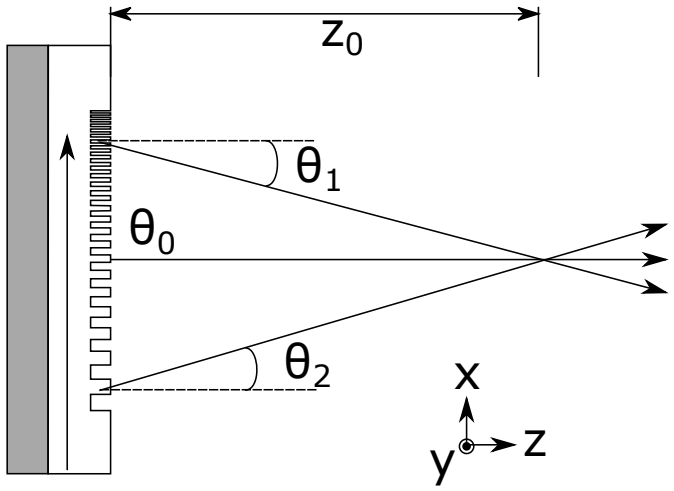

Figure 6.1: Illustration of chirped grating on planar waveguide

6.1 Chirped Grating Design

An example surface-relief, straight-line, chirped grating etched on a planar waveguide is shown in Fig. 6.1. Consider a guided mode traveling in the x-direction. The grating spatial frequency is a linear function of x so that the out-coupling rays intersect at a point a distance z_0 from the grating. By reciprocity, only the light from sources near the focal spot will efficiently couple into the guide. While it is possible to have the optical axis be non-normal to the waveguide surface, in this design the focal point and the center of the grating will be on the line $x = y = 0$. The surface of the grating will be defined to be $z = 0$. The sine of the angle required for a ray starting on the grating to come into focus is then given by

$$\sin\theta = \frac{-x}{\sqrt{x^2 + z_0^2}}. \tag{6.1}$$

Setting Eq. 6.1 equal to the grating equation 4.2, and solving for the grating period, yields

$$d = \lambda \frac{\sqrt{x^2 + z_0^2}}{n_{eff}\sqrt{x^2 + z_0^2} + x}. \tag{6.2}$$

The spatial frequency of the grating ξ is

$$\xi = \frac{1}{d} = \frac{1}{\lambda}\left(n_{eff} + \frac{x}{\sqrt{x^2 + z_0^2}}\right). \tag{6.3}$$

Assuming $z_0 >> L_g$, Eq. 6.3 can be approximated by

$$\xi \approx \frac{1}{\lambda}\left[n_{eff} + \left(\frac{x}{z_0}\right) - \frac{1}{2}\left(\frac{x}{z_0}\right)^3 + \frac{3}{8}\left(\frac{x}{z_0}\right)^5\right], \tag{6.4}$$

which is nearly linear in x.

Using same waveguide as the imaging skin, a chirped grating was designed for $\lambda = 632.8\,nm$. The focal length and grating width were chosen to $10\,cm$ and $1\,cm$ giving an $f/\#$ of 10. To verify Eq. 6.2, the grating was simulated using ray tracing. The grating period was sampled uniformly across the aperture and the out-coupling angle, θ, was calculated at each point. The rays, when extended, come to a focus at the designed focal length, as shown in Fig. 6.2.

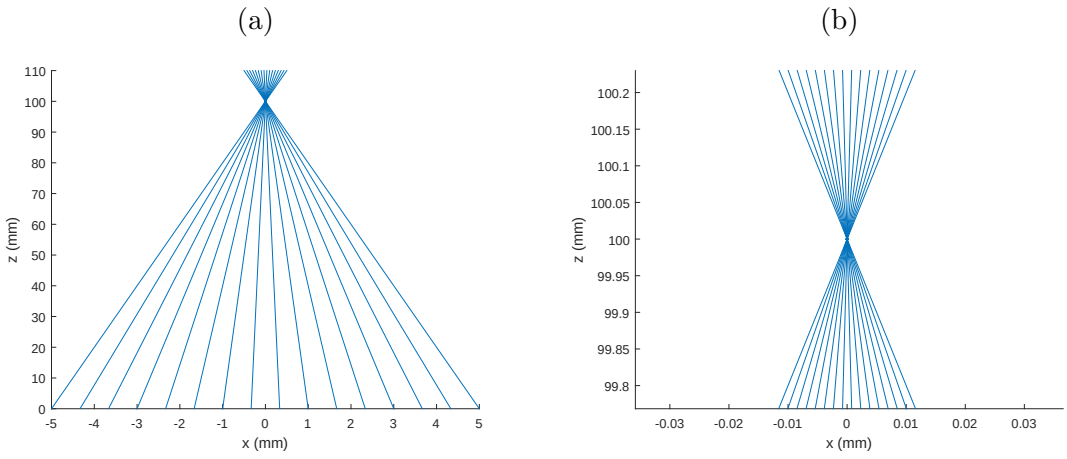

Figure 6.2: Ray trace of chirped grating coupler (a) and zoomed in version (b)

6.2 Chirped Grating Chromatic Dispersion

Like the uniform-period grating coupler, the resolution of the chirped grating is limited by chromatic dispersion. For example, the chirped grating designed for $\lambda = 632.8\,nm$

was simulated with $\lambda = 633.8\,nm$. From the ray trace shown in Fig. 6.3, the $1\,nm$ wavelength detuning shifted the best focus in x and z by $0.3\,mm$ and $0.15\,mm$ respectively. The spot size also appears to have increased to approximately $25\,\mu m$ at best focus.

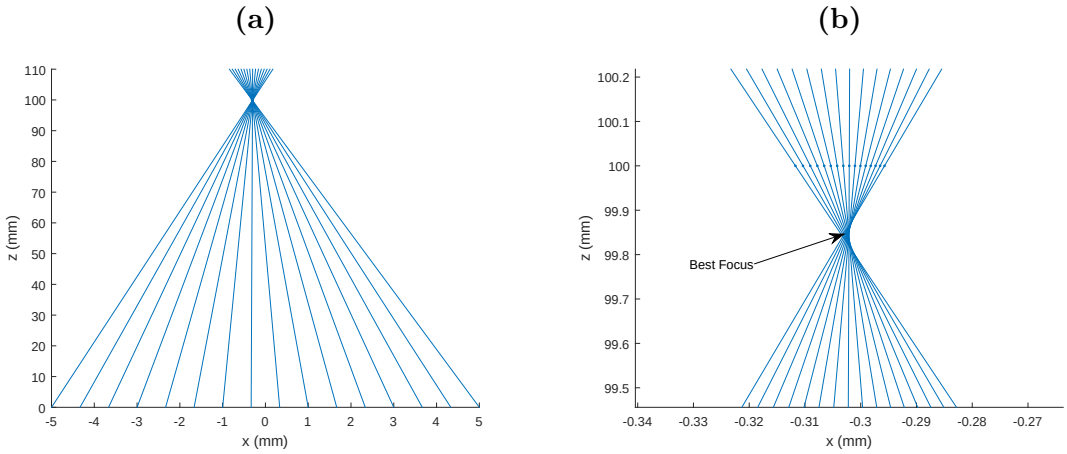

Figure 6.3: Ray trace of chirped grating coupler with $1\,nm$ wavelength detuning **(a)** and a zoomed in version **(b)**

Unlike the uniform period grating, the chromatic dispersion for chirped gratings does not have known analytic description. In the following analysis, the dispersion is determined numerically by repeating the ray tracing for a range on wavelengths. All of the rays leaving the grating have the form

$$x = z \tan\theta + x_0, \tag{6.5}$$

where x_0 is the position of the ray at the grating surface. We can represent all rays by the system of equations,

$$A \begin{bmatrix} x \\ z \end{bmatrix} = \vec{x}_0, \tag{6.6}$$

where each row of A and $\vec{x}_0$ represent one of the N simulated rays, and the matrix A is

$$A = \begin{bmatrix} 1 & -\tan\theta_1 \\ 1 & -\tan\theta_2 \\ \vdots & \vdots \\ 1 & -\tan\theta_N \end{bmatrix}. \tag{6.7}$$

The angle for each ray $theta_n$ is calculated using

$$\theta_n = \arcsin\left(n_e ff - q\frac{\lambda}{d_n}\right), \tag{6.8}$$

where d_n is the local grating period for the n^{th} ray. At the design wavelength, all rays come to a focus at a single spot which can be determined by solving Eq. 6.6 for $[x, z]^\top$. At other wavelengths, the rays do not share an intersection. The best focus, in a least-squares sense, is calculated by

$$\begin{bmatrix} x \\ z \end{bmatrix} = A^\dagger \vec{x_0}, \tag{6.9}$$

where $A^\dagger$ is the Moore-Penrose pseudo-inverse

$$A^\dagger = A^\top \left(AA^\top\right)^{-1}, \tag{6.10}$$

and $A^\top$ is the transpose of A.

The x and y-coordinates of the best focus location for a range of wavelengths is shown in Fig. 6.4. Chromatic dispersion for a focusing grating coupling results in a linear shift and misfocus. For this particular grating, a 5% change in wavelength results in a 5% change in best focus length and twice that distance translation in x position.

The spectral width is defined to be the change in wavelength which shifts the focus by one resolvable spot. The diffraction limit for this system is

$$\Delta x = \frac{\lambda z_0}{L_g}, \tag{6.11}$$

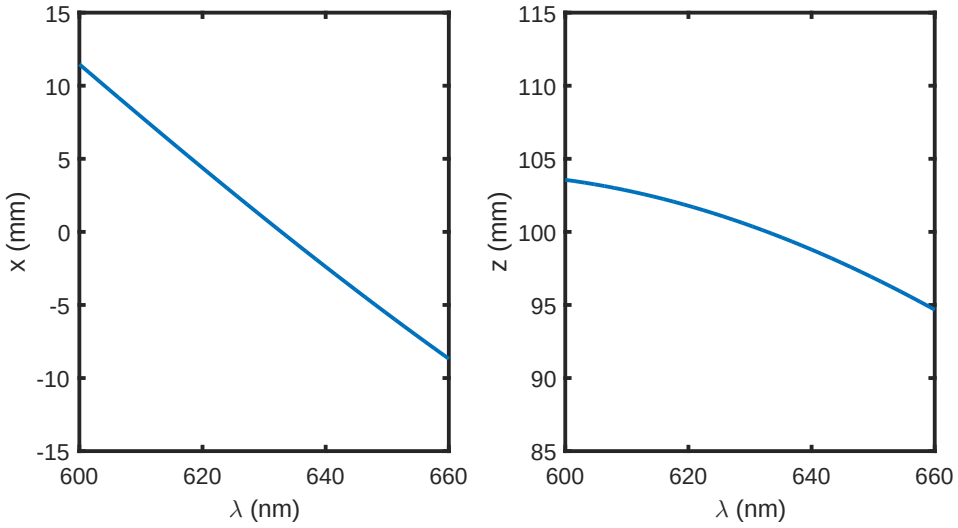

Figure 6.4: Best focus dispersion in the x **(a)** and z **(b)** directions

which for this particular grating at $\lambda = 632.8\,nm$ is $6.328\,\mu m$. Because the x-dispersion curve is linear near the design wavelength, the spectral width is

$$\Delta\lambda \approx \left(\frac{dx}{d\lambda}\right)^{-1} \Delta x. \tag{6.12}$$

The slope of the simulated x-direction dispersion curve at the design wavelength is -3.357×10^5, so the spectral width for this focusing coupler is $18.8\,pm$.

Recall that the spectral resolution for a linear grating coupler is

$$\left|\frac{\lambda}{\Delta\lambda}\right| = L_g \left(\frac{q}{d} - \frac{dn_eff}{d\lambda}\right). \tag{6.13}$$

One might then expect the spectral resolution in the x-direction to be in the range

$$L_g \left(\frac{1}{max(d)} - \frac{dn_eff}{d\lambda}\right) = 3.2734{\times}10^4 \leq \left|\frac{\lambda}{\Delta\lambda}\right| \leq 3.4313{\times}10^4 = L_g \left(\frac{1}{min(d)} - \frac{dn_eff}{d\lambda}\right) \tag{6.14}$$

The spectral resolution for this particular focusing grating coupler is 3.357×10^4, well within the expected range.

For a finite conjugate system, aberrations further limit to the allowed chromatic range compared to an infinite conjugate system. After removing the primary aberrations, namely linear shift and misfocus, the rays still do not come into a sharp focus for all but the design wavelength. The spot width (Δx) is defined as the full width in the x-direction of the interersections of the rays with the plane of best focus. The simulated width for each wavelength is plotted in Fig. 6.5. The spot is considered nearly diffraction limited if the spot width from ray tracing is less than twice the diffraction limit given in 6.11. For this particular design, the spot is nearly diffraction limited within the $20\,nm$ band around the design wavelength. Outside the chromatic range, the focusing grating-based imaging systems become highly aberrated and can not be corrected.

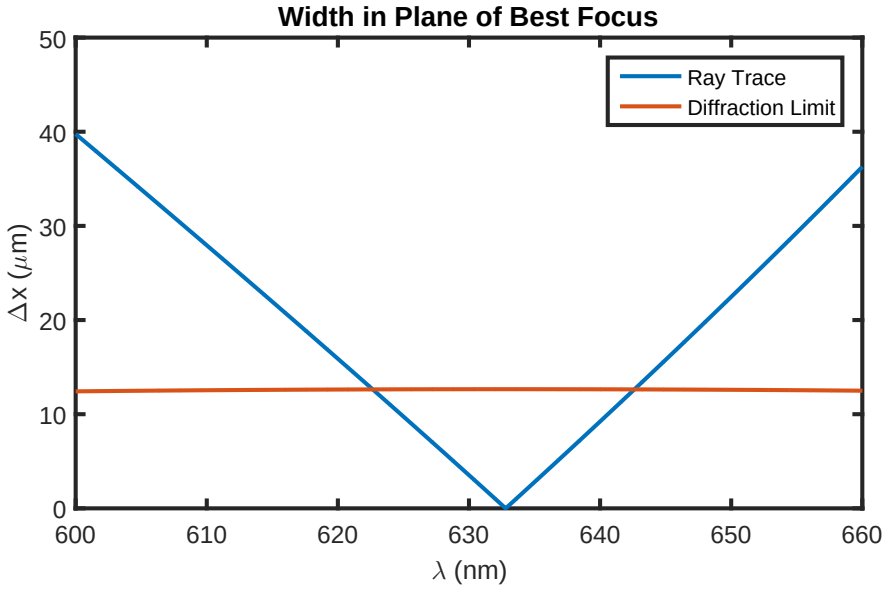

Figure 6.5: Spot size from ray tracing and the diffraction limit

6.3 Depth of Field

In a confocal imaging system, points off the object plane are highly attenuated. The same is true for finite conjugate imaging skins. Assuming a FGC maps a waveguide mode to a diffraction limited line, the complex amplitude of the out-coupling mode is

$$A(x) = A_0 \exp\left(-jk\sqrt{x^2 + (z - z_0)^2}\right) rect\left(\frac{x}{L_g}\right), \tag{6.15}$$

where A_0, the uniform magnitude, is related to the power in the mode. Similarly, the complex amplitude at the grating surface from a line source z_0' away is

$$B(x) = B_0 \exp\left(-jk\sqrt{x^2 + (z - z_0)^2}\right) rect\left(\frac{x}{L_g}\right). \tag{6.16}$$

The coupling efficiency of the power incident on the grating is given by the overlap integral

$$\eta(z_0, z_0') = \frac{\left|\int_{-\infty}^{\infty} A(x)B^*(x)dx\right|^2}{\int_{-\infty}^{\infty} |A(x)|^2\, dx \cdot \int_{-\infty}^{\infty} |B(x)|^2\, dx}. \tag{6.17}$$

If the object is a point and not a line, the single integrals and cylindrical wave terms would be replaced by double integrals and spherical waves respectively. Eq. 6.17 was evaluated numerically for the FGC described in the previous section. Fig. 6.6 shows the calculated efficiency as the designed object distance, z_0, was held constant and the actual object distance, z_0', was changed. The depth of field (DOF), defined to be the full width half max of the efficiency with respect to z_0', for this particular grating was $400\,\mu m$.

The DOFs for different object distances and grating lengths are shown in Fig. 6.7**(a)**. The DOF depends on the ratio of z_0 to L_g (the $f\#$), but not the individual values as shown in Fig. 6.7**(b)**. Similar to a standard lens which has a DOF equal to $\lambda(f/\#)^2$, the included fit shows that the depth of field for a FGC is a quadratic function of the $f/\#$.

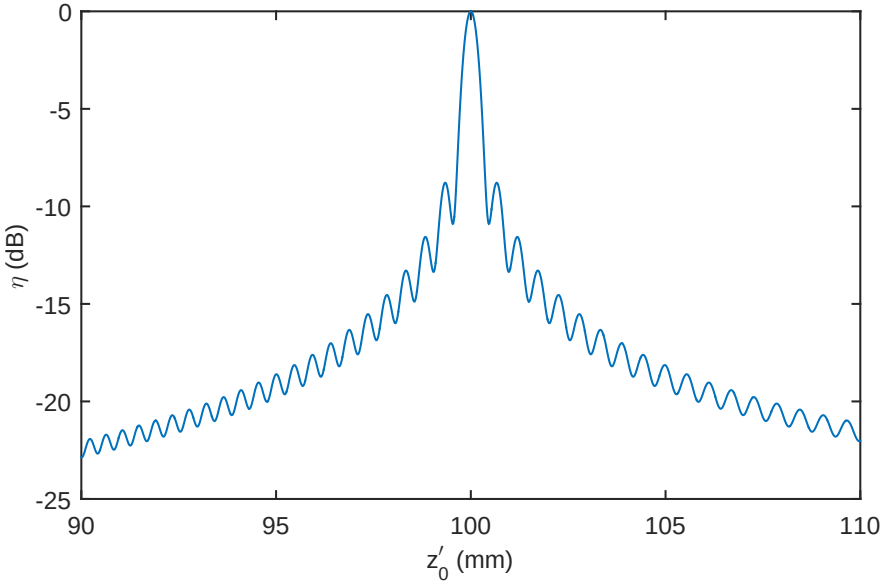

Figure 6.6: Coupling efficiency versus object distance for a straight-line chirped grating

6.4 Conclusions

Imaging skins and threads can be made to have any conjugate ratio. Unlike a lens, the object distance is set at fabrication and cannot be changed. Focusing grating couplers have additional chromatic dispersion compared to the uniform period gratings. Specifically, the focal length and spot width are functions of wavelength. This means a finite conjugate imaging skin is nearly diffraction limited over a very narrow spectral band. Like a confocal system, object points off the object plane are highly attenuated. This may be useful if one would like topographic information about the object. There exist other applications where it is preferable for out-of-focus objects to appear as blurred spots. In these cases, the spatial resolution needs to be reduced to increase the depth of field.

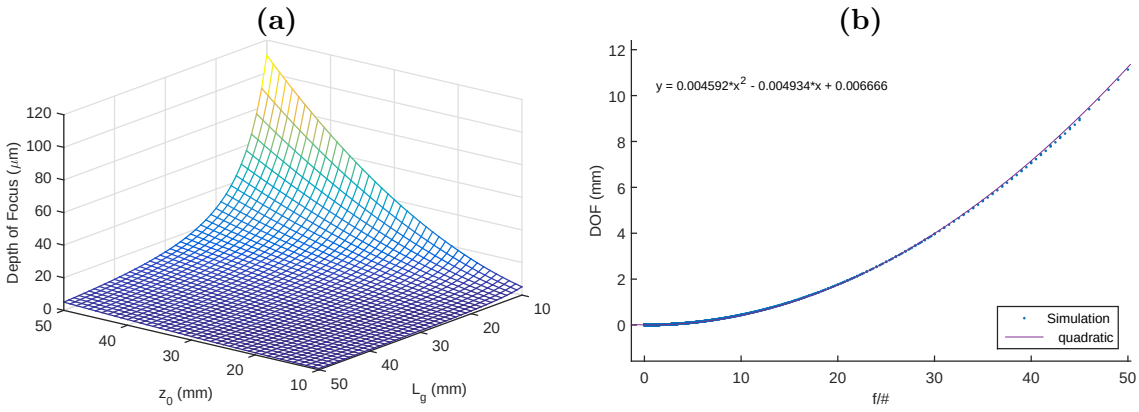

Figure 6.7: Depth of focus vs **(a)** grating length and object distance **(b)** $f/\#$

Chapter 7

Conclusions

The far-field resolution of any imaging system is proportional to the width of the aperture. The depth, however, depends on the system architecture. A system effectively confined to a plane, the so-called imaging skin, was presented. In this system, a grating coupler maps far-field points into guided waveguide modes. As long as the object point is further than the Rayleigh range from the grating surface, the coupling efficiency was shown to be as high as 80% that of a standard lens. Although only a few wavelengths thick, the imaging skin has a far-field resolution near the diffraction limit for a lens with a similar pupil width.

If high resolution is needed only in a single spatial-direction, the form-factor can be further reduced to be nearly one-dimensional. Similar to the imaging skin, the imaging thread uses a grating to map points in the far-field into a mode of a waveguide. In this case, the waveguide is an optical fiber and the coupler is a tilted fiber Bragg grating (TFBG). Using the side of the fiber instead of the end-facet allows for much greater far-field resolution, albeit in a single dimension, compared to other fiber imaging techniques. The point spread function of this system forms a segment of an ellipse in the object plane. Setting the grating tilt angle to 45°, the Bragg matched out-coupling angle is normal to

the fiber surface and the PSF becomes a line segment. The point coupling efficiency is inversely proportional to the length of the PSF and, therefore, significantly lower than an imaging skin with the same grating length. As a proof of concept, an imaging thread formed a one-dimensional image of the far-field from a Dammann grating.

The gratings in both imaging skins and threads have a high degree of chromatic dispersion. This requires either monochromatic illumination or the ability to separate the power into very narrow spectral bands. Specifically, the spectral resolution needed to maintain high spatial resolution is approximately equal to the number of grating lines. A second grating, a lens, and a detector array can be used as a spectrometer to measure each wavelength in parallel. If the object spectrum is known apriori, the wavelength encodes angle and no mechanical scanning is needed. If the system with the spectrometer is mechanically scanned, imaging skins and threads can build hyperspectral images.

Because of their narrow spectrum requirement and scanned image capture, imaging threads and skins have significantly lower optical throughput compared to a conventional lens based system. Assuming they can be isolated before detection, multiple guided spatial modes can add parallelism to the image capture. The spatial modes are analogous to the multiple apertures often used in confocal imaging. A second grating, a lens, and a detector array can be used to isolate the modes. The resolution of the second grating coupler can be much lower the imaging grating. Though this system is not strictly planar, the lens and detector can be made from thin micro-optics. The coupling efficiency of volume gratings, like the TFBG, is polarization sensitive. To use this multimode technique on an imaging thread, the polarization angle must be maintained between the two gratings. As a proof of concept, a dual prism coupler imaged a pseudo-random barcode using four independent modes.

Finite conjugate imaging is possible by adding a chirp to the grating period. Like a confocal system, finite conjugate imaging skins and threads only have high coupling

efficiency in a narrow depth of focus (DOF). The DOF is proportional to the $f/\#$ squared. Therefore, the depth over which a grating-based, finite conjugate system can detect an object is inversely proportional the square of the lateral resolution. In addition to the lateral chromatic dispersion, finite conjugate systems have an effective focal length and spot size which depend on wavelength. Therefore, a diffraction limited spot is only possible within an extremely narrow spectral range.

Through imaging skins and threads, it is possible to design imaging systems that are effectively confined to a plane or a line. This reduction of form factor has come at the expense of reduced optical throughput and increased chromatic dispersion. Despite these limitation, imaging skins and threads were able to form images at nearly their diffraction limits. The grating coupler on waveguide, therefore, represents the architecture with the smallest known form factor capable of this far-field resolution.

References

[1] Lord Rayleigh. On pin-hole photagraphy. 31, 1891.

[2] Joseph Goodman. *Introduction to Fourier Optics*. Roberts and Company, 2005.

[3] Henry C. King. *The history of the telescope*. Dover, 1979.

[4] Eric J. Tremblay, Ronald A. Stack, Rick L. Morrison, and Joseph E. Ford. Ultrathin cameras using annular folded optics. *Applied Optics*, 46(4):463–471, February 2007.

[5] D. W. Sweeney and G. E. Sommargren. Harmonic diffractive lenses. 34(14):2469–2475.

[6] H. Kogelnik. Coupled wave theory for thick hologram gratings. *Bell Syst. Tech. J.*, 48(9):2909–2947, 1969.

[7] C. Fabry and A. Perot. Theorie et applications d'une nouvelle methode de spectroscopie interferentielle. *Ann. Chim. Phys*, 16.7:115, 1899.

[8] M.L. Dakss, L. Kuhn, P. F. Heidrich, and B. A. Scott. Grating coupler for efficient excitation of optical guided waves in thin films. *Applied Physics Letters*, 16:523–525, 1970.

[9] M. L. Dakss, L. Kuhn, P. F. Heidrich, and B. A. Scott. Grating coupler for efficient excitation of optical guided waves in thin films. *Applied Physics Letters*, 16(12):523–525, June 1970.

[10] H. Kogelnik and T. P. Sonowski. Holographic thin film couplers. 49:1602–1608, 1970.

[11] S. T. Peng, Tamir T, and H. L. Bertoni. Theory of periodic dielectric waveguides. 23:123–133, January 1975.

[12] John C. Brazas and Lifeng Li. Analysis of input-grating couplers having finite lengths. *Applied Optics*, 34(19):3786–3792, July 1995.

[13] P. K. Tien. Light waves in thin films and integrated optics. 10:2395–2413, Nov. 1971.

[14] T. Tamir and S. T. Peng. Analysis and design of grating couplers. 14:235–25, 1977.

[15] D. Marcuse. Mode conversion caused by surface imperfectioins of a dielectric slab waveguide. 48:3187–3215, 1969.

[16] Dietrich Marcuse. *Theory of Dielectric Optical Waveguides*. Academic Press, 1972.

[17] D.H. Yoon, S.G. Yoon, and Y.T. Kim. Refractive index and etched structure of silicon nitride waveguides fabricated by pecvd. *Thin Solid Films*, 515:5004–5007, 2007.

[18] Curt A. Flory. Analysis of directional grating-coupled radiation in waveguide structures. *IEEE JOURNAL OF QUANTUM ELECTRONICS*, 40:949–957, July 2004.

[19] William Streifer, Don R. Scifres, and Robert D. Burnham. Analysis of grating-coupled radiation in gaas:gaalas lasers and waveguides. *IEEE Journal of Quantum Electronics*, 12(7):422–428, July 1976.

[20] J. K. Butler, W. E. Ferguson Jr.and Gary A. Evans, and P. J. Stabile. A boundary element technique applied to the analysis of waveguides with periodic surface corrugations. *IEEE J. Quantum Electron*, 28(7):1701–1709, July 1992.

[21] Stephen A. Campbel. *Fabrication Engineering*. Oxford University Press, third edition.

[22] A. Stoffel, A. Kovacs, W. Kronast, and B. M. Muller. Lpcvd against pecvd for micromechanical applications. 6:1–6, 1996.

[23] P. E. Jessop J. D. B. Bradley and A. P. Knights. Silicon waveguide-integrated optical power monitor with enhanced sensitivity at 1550 nm. *Applied Physics Letters*, page 241103, 2005.

[24] E. Marom, B. Chen, and 0. G. Ramer. Determination of ray directions coupled out of waveguides through prisms and gratings. *Applied Optics*, 18(7):1092–1096, April 1979.

[25] G. Meltz, W. W. Morey, and W. H. Glenn. Formation of bragg gratings in optical fibers by a transverse holographic method. 14(15):823–825, 1989.

[26] J. Albert, L. Y. Shao, and C. Caucheteur. Tilted fiber bragg gratings sensors. *Laser Photonics Review*, 7:83–108, 2013.

[27] Tomas Cizmar and Kishan Dholakia. Exploiting multimode waveguides for pure fibre-based imaging. *Nature Communications*, 3:1–9, 2012.

[28] Barmak Heshmat, Ik Hyun Lee, and Ramesh Raskar. Optical brush: Imaging through permuted probes. *Scientific Reports*, 6:1–9, 2015.

[29] G. J. Tearney, S. A. Boppart, B. E. Bouma, M. E. Brezinski, N. J. Weissman, J.F. Southern, and J. G. Fujimoto. Scanning single-mode fiber optic catheter-endoscope for optical coherence tomography. *Optics Letters*, 21(7):543–545, 1996.

[30] Min Gu, Hong Kang, and Xiangping Li. Breaking the diffraction-limited resolution barrier in fiber-optical two-photon fluorescence endoscopy by an azimuthally-polarized beam. *Scientific reports*, 4:1–6, 2014.

[31] Yicong Wu, Yuxin Leng, Jiefeng Xi, and Xingde Li. Scanning all-fiber-optic enomicroscopy system for 3d nonlinear optical imaging of biological tissues. *Optics Express*, 17(10):7907–7915, 2009.

[32] Keiser. *Optical Waveguides*. 1972.

[33] W.X. Xie and et. al. Second order diffraction efficiency of bragg gratings written within germanosilicate fibres. 101:85–91, 1993.

[34] T. Erdogan and J. E. Sipe. Radiation-mode coupling loss in tilted fiber phase gratings. *Optics Letters*, 20(18):1838–1840, 1995.

[35] Yufeng Li, Mark Foggatt, and Turan Erdogan. Volue current method for analysis of tilted fiber gratings. *Journal of Lightwave Technology*, 19(10):1580–1585, October 2001.

[36] Herbert R Philipp. Optical properties of silicon nitride. 120(2):295–300, 1973.

[37] I. H. Malitson. Interspecimen comparison of the refractive index of fused silica. 55(10):1205–1209, 1965.

[38] M. J. Dodge. *Handbook of Laser Science and Technology*, volume IV. CRC Press, 1986.

[39]

[40] C. Lin, H. Kogelnik, and L. G. Cohen. Optical-pulse equalization of low-dispersion transmissionin single-mode fibers in the 1.3 um 1.7 um spectral region. 5(11), 1980.

[41] L. Grüner-Nielsen, S. Knudsen, B. Edvold, T. Veng, D. Magnussen, C. Larsen, and H. Damsgaard. Dispersion compensating fibers. *Optical Fiber Technology*, 6(2):164–180, 2000.

[42] Frdric Gerome, J.-L. Auguste, and J.-M. Blondy. Design of dispersion-compensating fibers based on a dual-concentric-core photonic crystal fiber. 29(23):2725–2727.

[43] K. E. Spaulding and G. M. Morris. Achromatic waveguide input/output coupler design. 30(9):1096–1112, 1991.

[44] T. Erdogan. 15(8):1277–1294.

[45] Raman Kashyap. *Fiber Bragg Gratings*. Academic Press, 1999.

[46] Ivan Avrutsky, Kalyani Chaganti, Ildar Salakhutdinov, and Gregory Auner. Concept of a miniature optical spectrometer using integrated optical and micro-optical components. *Appl. Opt.*, 45(30):7811–7817, Oct 2006.

[47] P. Cheben, J. H. Schmid, A. Delâge, A. Densmore, S. Janz, B. Lamontagne, J. Lapointe, E. Post, P. Waldron, and D.-X. Xu. A high-resolution silicon-on-insulator arrayed waveguide grating microspectrometer with sub-micrometer aperture waveguides. *Opt. Express*, 15(5):2299–2306, Mar 2007.

[48] Bruno Martin, Alain Morand, Pierre Benech, Gregory Leblond, Sylvain Blaize, Gilles Lerondel, Pascal Royer, Pierre Kern, and Etienne Le Coarer. Design of a

compact static fourier transform spectrometer in integrated optics based on a leaky loop structure. *Opt. Lett.*, 34(2):184–186, Jan 2009.

[49] L. A. Coldren. Monolithic tunable diode lasers. *IEEE Journal of Selected Topics in Quantum Electronics*, 6(6):988–999, 2000.

[50] G. Q. Xiao, T. R. Corle, and G. S. Kino. Realtime confocal scanning optical microscope. *Applied Physics Letters*, 53(8):716–718, February 1988.

[51] H. O. Bartlet and A. W. Lohmann. Mode analysis of optical fibres using computer-generated matched filters. 1983.

[52] Victor Soifer and Mikhail Golub. *Laser Beam Mode Selection by Computer Generated Holograms*. CRC Press, 1994.

[53] A. Katzir, A. C. Livanos, and A. Yariv. Chirped-grating output couplers in dielectric waveguides. 30(5):225–226, 1977.

[54] M. Miler and M. Skalsky. Chirped and curved grating coupler focusing both outgoing beam and guided wave. 33(1):13–16, 1980.

[55] D. Heitmann and C. Ortiz. Calculation and experimental verification of two-dimensional focusing grating couplers.

[56] Eugene Hecht. *Optics*. Pearson Education, 4th ed. edition, 2002.

Appendix A

Derivation of Minimum Lens System Depth

The total width of a single lens imaging system includes the image distance and the thickness of the lens' dielectric material. The lens sag and image distance are inversely related; both distances can not simultaneously be made arbitrarily small. The following analysis determines the minimum system width and the focal length at which this minimum occurs. Two assumptions are made to simplify the analysis. The imaging system is used at infinite conjugates, $d_i = f$, and the lens is plano-convex. A diagram of the system is shown in Fig. A.1.

The total system thickness, from the leftmost surface of the lens to the image plane, is

$$T = f + d - h2, \tag{A.1}$$

where f is the focal length, d is the lens thickness, and $h2$ is the distance from the lens surface to the second principle plane. The minimum thickness for any convex refractive lens is its sag, s, which here after will be used in place of d. Lens sag, which is the difference between the thickest and thinnest sections of the lens, depends on the lens

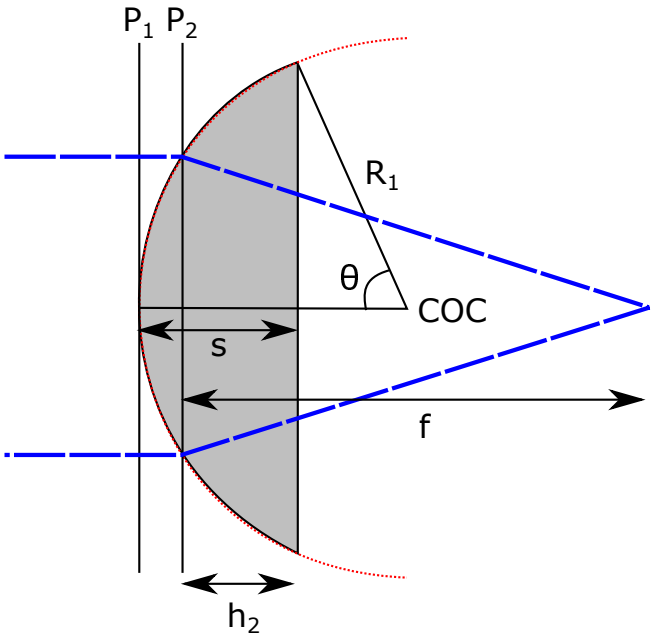

Figure A.1: Sag of a plano-convex lens

diameter and the radius of curvature. The relationship between the index of refraction (n), focal length (f), and the radii of curvature (R_1 and R_2) for any lens in air is given by the lens makers equation,

$$\frac{1}{f} = (n-1)\left[\frac{1}{R_1} - \frac{1}{R_2} + \frac{(n-1)d}{nR_1R_2}\right]. \tag{A.2}$$

Under the plano-convex assumption, R_2 approaches infinity. Taking the limit and solving Eq. A.2 for R_1 yields,

$$R_1 = (n-1)f. \tag{A.3}$$

By definition, all of the points on the convex surface are a distance R_1 from the center of curvature (COC). The sag of a plano-convex lens is given by

$$s = R_1 - R_1\cos\theta, \tag{A.4}$$

where θ is the projection angle of the lens aperture. For a lens of diameter D, this angle

is

$$\cos\theta = \frac{\sqrt{R_1^2 - D^2/4}}{R_1} \tag{A.5}$$

Substituting Eq. A.5 in A.4 yields

$$s = R_1 - 1/2\sqrt{4R_1^2 - D^2}. \tag{A.6}$$

The distance from the second principal plane to the lens surface is given by [56] to be

$$h_2 = \frac{f(n-1)d}{nR_1}. \tag{A.7}$$

After substituting Eqs. A.7 and A.6 and some simplification, Eq. A.1 becomes

$$T = f\left[1 + \frac{(n-1)^2}{n}\right] + \frac{(n-1)}{2n}\sqrt{4f^2(n-1)^2 - D^2}] \tag{A.8}$$

Setting the derivative of Eq. A.8 equal to zero and solving for f,

$$f = \pm D\frac{n^2 - n + 1}{2(n-1)\sqrt{2n^3 - 3n^2 + 2n}} \tag{A.9}$$

Because we are only concerned with the case where the light comes to a real focus, the negative term can be ignored. To ensure that this stationary point is a minimum, the second derivative was calculated and found to be positive. For a lens with index of 1.5, the minimum focal length is approximately equal to the lens diameter. Evaluating Eq. A.8 for this value of the focal length,

$$T_{min} = D\frac{\sqrt{2n^3 - 3n^2 + 2n}}{2n^2 - 2n} \tag{A.10}$$

The total thickness of an infinite-conjugate imaging system using a single plano-convex lens is minimized when the focal length is on the order of the lens diameter. The constant of proportionality is a monotonic function of the lens' refractive index and is very nearly unity for an index of 1.5. When the index is 2, the maximum for common lens materials in the visible band, the depth decreases by a factor of $\sqrt{2}$. At this index,

the total system depth is approximately 10% larger than the lens diameter. As $n \to \infty$, the minimum thickness approaches

$$T_{min} \approx \frac{D}{\sqrt{2n}}. \tag{A.11}$$

Although increasing the refractive index reduces the minimum thickness, it does so very slowly.

Appendix B

Derivation of TFBG Radiation Pattern

It has been shown that the radiation modes from a tilted fiber Bragg grating (TFBG) propagate along the edge of a cone. This cone intersects the object plane forming an ellipse. The parameterized equations describing that ellipse are derived.

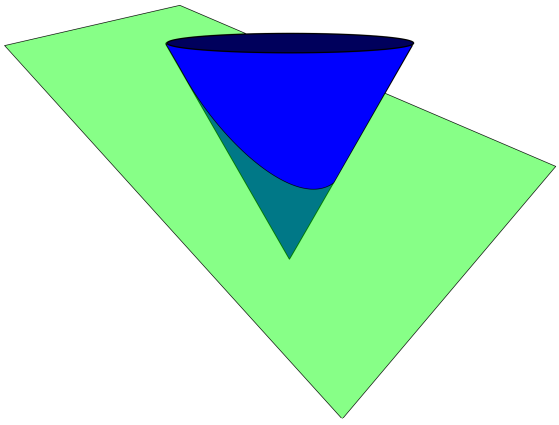

Figure B.1: Cartoon of cone intersecting object plane

The cone, shown in figure B.1, can be parameterized by the system of equations

$$\begin{aligned} x &= R\sin\theta\cos\phi \\ y &= R\sin\theta\sin\phi \\ z &= R\cos\theta, \end{aligned} \tag{B.1}$$

where R and ϕ are the free parameters, but θ is a constant.

The object plane was chosen such that its normal, the image axis, is along the cone at $\phi = 0$. Because its x and z coordinates are independent of y, the object plane can be described by a system of equations of the form

$$\begin{cases} x = x \\ y = y \\ z = f(x) \end{cases} . \tag{B.2}$$

The determination of $f(x)$ is a 2D problem as shown in figure B.2.

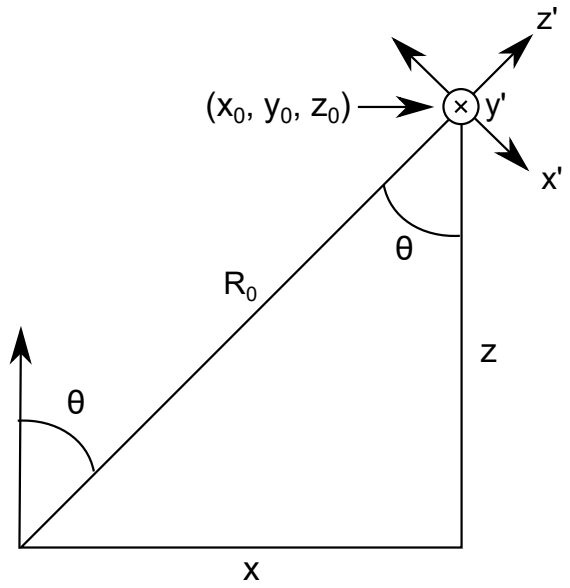

Figure B.2: 2D view of cone-plane intersection

For the image axis, x and z are related by

$$\tan\theta = \frac{x}{z} \tag{B.3}$$

or

$$z = \frac{1}{\tan\theta}x. \tag{B.4}$$

Because they are orthogonal, the slope of the object plane will be the negative inverse the slope of the image axis, explicitly

$$m_{op} = -\tan\theta. \tag{B.5}$$

The origin of the object plane can be calculated by setting $\phi = 0$ and $R = R_0$ in eq. B.1 which is

$$\begin{bmatrix} x_0 \\ y_0 \\ z_0 \end{bmatrix} = \begin{bmatrix} R_0\sin\theta \\ 0 \\ R_0\cos\theta \end{bmatrix}. \tag{B.6}$$

Knowing the slope and a point, one can calculate the intercept which is

$$b = z_0 - m_{op}x_0 = R_0\left(\cos\theta + \tan\theta\sin\theta\right). \tag{B.7}$$

The z of the object plane is then given by

$$z = f(x) = -\tan\theta x + R_0\left(\cos\theta + \tan\theta\sin\theta\right). \tag{B.8}$$

Substituting eq. B.1 in eq. B.8 one arrives at

$$R\cos\theta = -\tan\theta R\sin\theta\cos\phi + R_0\cos\theta + R_0\tan\theta\sin\theta. \tag{B.9}$$

After solving for R and some simplification, eq. B.9 becomes

$$R = \frac{R_0}{\cos^2\theta + \sin^2\theta\cos\phi}. \tag{B.10}$$

Parameterized equations describing the radiation pattern can be calculated by substituting eq. B.10 in eq. B.1 yielding

$$\begin{cases} x = R_0 \frac{\sin\theta\cos\phi}{\cos^2\theta + \sin^2\theta\cos\phi} \\ y = R_0 \frac{\sin\theta\sin\phi}{\cos^2\theta + \sin^2\theta\cos\phi} \\ z = R_0 \frac{\cos\theta}{\cos^2\theta + \sin^2\theta\cos\phi} \end{cases} . \tag{B.11}$$

However, these are in terms of the grating coordinate system (x, y, z) rather than a convenient object plane system (x', y', z'). z' is in the direction of the imaging axis. x' and y' are the directions corresponding to an infinitesimal change in θ and ϕ respectively at the origin. $\hat{y'}$ is parallel to y,

$$y' = [0, 1, 0] \begin{bmatrix} x - x_0 \\ y - y_0 \\ z - z_0 \end{bmatrix} . \tag{B.12}$$

The unit vector parallel to any line of the form $z = mx + b$ can be calculated by

$$\hat{l} = \frac{[x_2, 0, mx_2] - [x_1, 0, mx_1]}{\sqrt{(x_2 - x_1)^2 + m^2 (x_2 - x_1)^2}} \tag{B.13}$$

$$= \frac{1}{\sqrt{1 + m^2}} [1, 0, m] . \tag{B.14}$$

The slopes for $\hat{x'}$ and $\hat{z'}$ are $-\tan\theta$ and $1/\tan\theta$ respectively.

$$\hat{x'} = \frac{1}{\sqrt{1 + \tan^2\theta}} [1, 0, -\tan\theta] \tag{B.15}$$

$$\hat{z'} = \frac{1}{\sqrt{1 + \cot^2\theta}} [1, 0, \cot\theta] \tag{B.16}$$

Using the trigonometric identities $1 + \tan^2\theta = \sec^2\theta$ and $1 + \cot^2\theta = \csc^2\theta$,

$$x' = [\cos\theta, 0, -\sin\theta] \begin{bmatrix} x - x_0 \\ y - y_0 \\ z - z_0 \end{bmatrix}. \tag{B.17}$$

$$z' = [\sin\theta, 0, \cos\theta] \begin{bmatrix} x - x_0 \\ y - y_0 \\ z - z_0 \end{bmatrix}. \tag{B.18}$$

The difference vector is given by

$$\begin{bmatrix} x - x_0 \\ y - y_0 \\ z - z_0 \end{bmatrix} = R_0 \begin{bmatrix} \sin\theta \left(\frac{\cos\phi}{\cos^2\theta + \sin^2\theta\cos\phi} - 1 \right) \\ \frac{\sin\theta\sin\phi}{\cos^2\theta + \sin^2\theta\cos\phi} \\ \cos\theta \left(\frac{1}{\cos^2\theta + \sin^2\theta\cos\phi} - 1 \right) \end{bmatrix}. \tag{B.19}$$

Substituting eq. B.19 in eqs. [B.17, B.12, B.18 yields

$$\begin{cases} x' = \frac{R_0}{2} \frac{(\cos\phi - 1)\sin 2\theta}{\cos^2\theta + \sin^2\theta\cos\phi} \\ y' = R_0 \frac{\sin\phi\sin\theta}{\cos^2\theta + \sin^2\theta\cos\phi} \\ z' = 0 \end{cases}. \tag{B.20}$$

As designed, all points lie in the object plane spanned by (x', y').